IMPACT OF WIND ENERGY ROTOR WAKES ON FIXED-WING AIRCRAFT AND HELICOPTERS

Berend G. van der Wall, berend.vanderwall@dlr.de, DLR (Germany)
Dietrich Fischenberg, dietrich.fischenberg@dlr.de, DLR (Germany)
Paul H. Lehmann, paul.lehmann@dlr.de, DLR (Germany)
Lennert B. van der Wall, l.vanderwall@tu-bs.de, TU Braunschweig (Germany)

Abstract

The wake of wind energy rotors is modeled as a tip vortex helix with a vortex strength estimated from its rotor thrust. A fixed-wing sail plane and a helicopter whose rotor is represented as a fixed-wing circular disk (instead of rotating blades) are subjected to the wake. In both cases the roll moment induced by the wake is compared to the maximum roll control moment of the aircraft. For comparison with revolving blades, the blade element momentum theory is applied to the isolated rotor and a simulation of an entire helicopter is used as well. It is found that typical on-shore power plants could be a hazard for sailplanes, but not for helicopters. Large off-shore wind energy converters, however, could even be a danger for small helicopters that may be used for maintenance.

NOMENCLATURE

A, B	Non-dimensional effective begin and end of rotor blade, referenced to R
A	Rotor disk area, m²
b	Wing span, m
c, c_{eq}	Airfoil chord and equivalent chord, m
C_l, C_L	Blade element and aircraft lift coefficient
$C_{l\alpha}$	Lift curve slope
$C_{l,W}$	Wake-induced roll moment coefficient
$C_T, C_{T,WE}$	Thrust coefficients of helicopter rotor and wind energy turbine
c_n	Radial integral coefficients, $n = 0,1,2, \ldots$
$d_0, d_C,$ d_S, d_W	Integral lift coefficients related to $\Theta_0, \Theta_C, \Theta_S, \lambda_{W0}$
$e_0, e_C,$ e_S, e_W	Integral moment coefficients related to $\Theta_0, \Theta_C, \Theta_S, \lambda_{W0}$
f_W	Spanwise lift weighing funciton
$L, \overline{L}$	Blade lift, N; non-dimensional blade lift
$M_\beta, \overline{M_\beta}$	Aerodynamic flap moment about the flapping hinge, Nm; non-dimensional flap moment
N_b	Number of rotor blades
r	Non-dimensional radial coordinate
R_c, r_c	Vortex core radius, m; non-dimensional core radius, referenced to R
R	Helicopter rotor radius, m
RCR	Roll control ratio
T, T_{WE}	Thrust of the helicopter rotor and the wind energy turbine, N
u, v, w	Velocity components in x, y, z directions, m/s
U	Rotor blade tip speed, m/s
v_{iW}	Wake vortex induced velocity, m/s
V_{iz}	Induced velocity normal to rotor disk, m/s
V_T, V_P	Non-dimensional velocities acting tangential and normal at the blade element, referenced to U
V_W	Wind speed, m/s
V_∞	Aircraft flight speed, m/s
x, y, z	Hub-fixed coordinates, x pos. downstream, y pos. starboard, z pos. up, m
Y_0, y_0	Vortex position within the rotor disk, m; non-dimensional position, referenced to R
α, α_W	Angle of attack, wake-induced angle of attack, deg
β_V	Core radius shape factor
Γ	Wind turbine tip vortex circulation strength, m²/s
Δ	Perturbation of a variable
δ_a	Aileron deflection, deg
$\Theta, \Theta_0,$ Θ_C, Θ_S	Blade section pitch angle, collective, lateral and longitudinal control angle, deg
Λ	Wing aspect ratio
λ_i	Thrust-induced inflow velocity normal to the rotor disk, non-dimensionalized by U
$\lambda_W,$ λ_{W0}	Wind turbine wake-induced inflow ratio and its amplitude, normal to the rotor disk, non-dimensionalized by U
μ	Rotor advance ratio, $\mu = V_\infty \cos\alpha / U$
μ_z	Axial inflow ratio, $\mu_z = -\mu \sin\alpha$
ρ	Air density, kg/m³
σ	Rotor solidity, $\sigma = N_b c/(\pi R)$
ψ	Rotor blade azimuth, deg
ψ_V	Wake age in terms of azimuth behind the blade, deg
Ω, Ω_{WE}	Rotor rotational speed of helicopter rotor and wind energy turbine, rad/s

1. INTRODUCTION

The sequencing of take-off and landing at airports are governed by safety requirements that emerge largely from wake interaction hazards. The strong wake vortices of preceding aircraft can have severe consequences on the following aircraft, exceeding their control capability with fatal consequences. Not only large and heavy aircraft such as wide bodies like a Boeing 747 or Airbus A380 can generate such dangerous strong tip vortices, even smaller aircraft like the Antonov AN-2 with 5.5 tons maximum gross weight caused a fatal accident with a following smaller Robin DR400-180 vehicle of 1 ton gross weight due to wake vortex encounter [1].

Numerous investigations concerning the effects of rotorcraft encountering the wake vortex of fixed-wing aircraft have been conducted in the past decades. In the 1980s, NASA [2] and US Army [3] investigated medium sized helicopters flying through wake vortices of airplanes using both flight testing and analytical methods. A UH-1H helicopter trimmed at 60 kts was used to fly through the wake vortices of a Douglas C-54 airplane at varying distances. Over the range of 0.42 nm to 6.64 nm, maximum rotor blade structural loads, helicopter attitude response and tail rotor flapping were measured. For these distances the helicopter reactions due to the wake were recognized but did not constitute safety hazards.

Numerical simulation was used in [4] and [5] to investigate the effects from a pair of trailing vortices of a preceding large airplane on the flight dynamics of a fixed and a rotary wing aircraft. The responses of airplane and helicopter are described as different in a way that the helicopter reacts more damped to the disturbance by the tip vortex.

More recently, work has been conducted by the University of Liverpool and QinetiQ, [6]-[8]. They investigated the influence of an active runway from an international airport to helicopter operations from a nearby approach and takeoff area. For their work they used flight mechanics simulation tools to examine the effects when a helicopter encounters the shed tip vortex from a large aircraft. A model of the vortex velocity profile was established by the use of LIDAR measurement data from the airport. Several calculations for the Lynx helicopter and forward speeds from hover to 80 kts were conducted. The results showed that the helicopter reaction is primarily dependent on the rotor position relative to the vortex center. In some combinations, hazardous helicopter reactions were recognized. The main question is, whether a rotorcraft which meets handling performance standards is able to recover the disturbed flight attitude after encountering the vortex.

The number of wind energy (WE) power plants on the country side in Germany is huge and many are in notable proximity to airfields. Recently this triggered investigation initially regarding the wake vortex hazard for sail planes encountering WE turbine wakes. The downstream wake of such horizontal axis WE turbines is characterized by a spiral helix of usually three blade tip vortices on the surface of the wake tube, as the number of blades is three for the overwhelming majority of the installed systems. This wake generates two different disturbances inside the tube and in the immediate vicinity of the tube itself. The tip vortex spiral on the surface of the tube is fed with circulation from the WE turbine blades and around each of these vortices induced swirl velocities are generated that induce velocities towards the turbine inside the tube – resulting in a global wind deficit – and adding on the wind velocity outside the tube.

Thus, inside the tube a global “wind deficit” is present that manifests itself as a loss of air momentum. Crossing the tube horizontally into its center will therefore generate a side-slip angle for the aircraft when penetrating the wake tube boundary on one side and this side-slip angle vanishes again when penetrating the wake tube boundary on the opposite side. At the boundary of the wake large horizontal vortex swirl velocities are encountered that change their sign at the boundary itself, representing a dual lateral pulse for the aircraft entering it.

The situation is very different when crossing the wake tube at its upper or lower boundary, i.e., in the immediate vicinity of the center of these vortices. In these cases the rotational swirl field of the vortices generates strong vertical velocities acting on the airplane’s wings. Depending on the aircraft size relative to the wake vortex spacing as well as to the proximity to the vortex centers, one wing may be subjected to upwash and the other one to downwash at the same instance of time, generating a large roll moment. Here, two scenarios come into mind: one, where the fuselage center line hits the vortex axis center; and one, where the fuselage is in the middle between two successive vortex centers. In the former case the vortex peak swirl velocities will be close to the middle of the fuselage with asymptotic decay towards the wing tips and in the latter case the peak swirl velocities affect the wing tips with decay towards the fuselage. Both cases can be considered as potentially hazardous.

The WE turbine wake and the wake-rotor interactional problem are illustrated in Fig. 1, showing the staggered vortices of the wake spiral and a helicopter approaching it from the right (a). The interactional problem of a rotor passing the upper end of the wake spiral in almost normal direction to it can be treated in different ways. In a first simplified approach the rotor may be viewed as a circular disk and handled like a wing of small aspect ratio, (b). In this case the turbine’s blade tip vortex has a stationary position on the wing and generates upwash with

increased wing lift on left of its center and downwash with accordingly less lift on the right of it. A refined model with four individual rotor blades is shown in (c). In this case the problem is unsteady in general because the rotating blades enter and pass the turbine's tip vortex induced velocity field during their revolution. Thus, the mathematical treatment is much more involved.

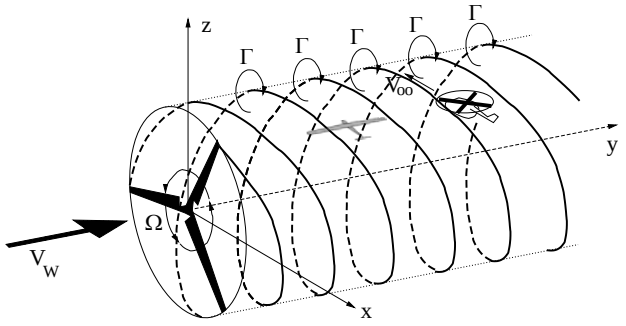

(a) Sketch of a WE turbine's wake with aircraft

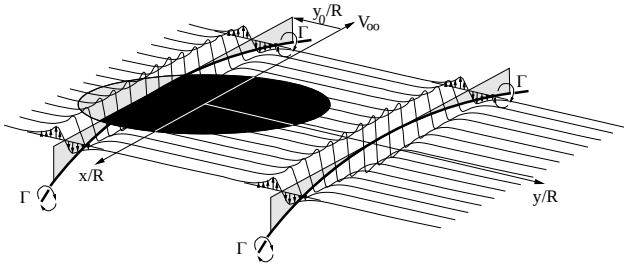

(b) Circular wing in WE turbine wake

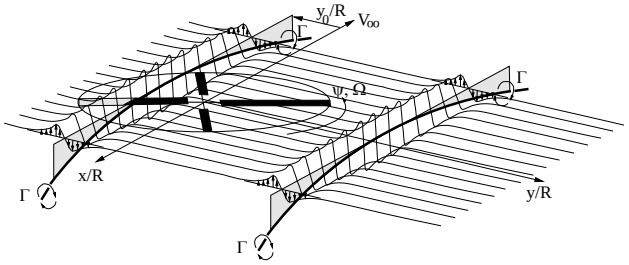

(c) Helicopter rotor in WE turbine wake

Fig. 1: Sketch of the WE turbine wake – rotor interaction problem.

2. TECHNICAL APPROACH

2.1. The wind turbines and the wake model

The investigations of this paper focus on two WE turbines of different power class: a representative on-shore 3 MW turbine and a representative off-shore 7 MW turbine. The reference chord at 93% radius is used to define the initial tip vortex core radius, while the equivalent solidity of the WE rotors is based on the thrust-weighted chord distribution. The helicopter investigated in this paper is the Bo105, representative for the 2-2.5 ton class. Data for the WE turbines and the helicopter are given in Table 1. The "worst case" scenario is of interest, which is the operational condition of the WE turbines with maximum tip vortex circulation strength which can be estimated from the rotor thrust coefficient.

Table 1: Dimensions and properties of the helicopter rotor and of the WE turbine rotors.

Rotor	Bo105	3 MW	7 MW
R, m	4.91	56.5	77.0
RPM	424	7-14	5-11
$V_{W,\Omega min}$, m/s	-/-	3-5	3-5
$V_{W,\Omega max}$, m/s	-/-	13	12
Ω, rad/s	44.4	0.733-1.466	0.524-1.152
U, m/s	218.0	41.4-82.8	40.3-88.7
$c(0.9R)$,m	0.270	1.000	1.363
c_{eq}, m	0.270	1.684	2.295
N_b	4	3	3
σ	0.070	≈ 0.0285	≈ 0.0285

It must be mentioned here that the definition of a rotor thrust coefficient in WE terms is different from that used in the helicopter community. In WE terms the reference dynamic pressure is based on half of the air density and the wind speed, $(\rho/2)V_W^2$, but in helicopter analysis the equivalent dynamic pressure is based on the air density and blade tip speed: ρU^2.

$$C_{T,WE} = \frac{T_{WE}}{(\rho/2)V_W^2 A_{WE}} \qquad C_T = \frac{T_{WE}}{\rho A_{WE} U_{WE}^2}$$
$$\Rightarrow C_T = \frac{1}{2}\left(\frac{V_W}{U_{WE}}\right)^2 C_{T,WE} \tag{1}$$

The specific blade loading, defined as C_T/σ, is an indicator in helicopter rotor analysis for the beginning of aerodynamic stall onset somewhere along the rotor blade when it exceeds a value of 0.12. From the definition of the specific blade loading the tip vortex strength can be estimated by means of lifting line theory as [9]:

$$\Gamma = 2U_{WE}c_{WE}\frac{C_T}{\sigma} = \frac{2\pi}{N_b}U_{WE}R_{WE}C_T$$
$$= \frac{\pi}{N_b}\frac{V_W^2}{\Omega_{WE}}C_{T,WE} \tag{2}$$

The thrust coefficients of WE turbines as a function of wind speed for the 3 MW turbine investigated here is shown by the dotted line in Fig. 2. Combined with the rotational speed of the turbines, the tip vortex circulation strength can be evaluated by Eq. (2) and is shown in Fig. 2 as solid line for the 3 MW turbine and as dashed line for the 7 MW turbine. It can be seen that a wind speed of $V_W = 10\,\mathrm{m/s}$ provides the largest value of tip vortex circulation, therefore this condition is used in the analysis of helicopter rotor trim.

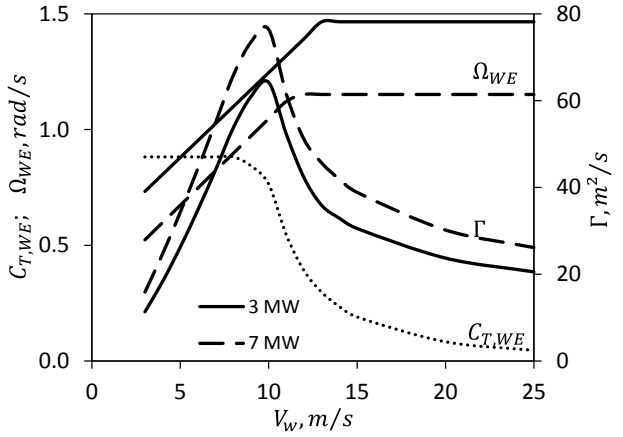

Fig. 2: WE turbine operational parameters and resulting tip vortex circulation strength.

Using the value of $C_{T,WE} = 0.764$ given (which corresponds to $C_T = 0.00758$ and $C_T/\sigma = 0.266$ in helicopter notation; this indicates that some portion of the blade is in a stalled condition) the peak circulation strength results in $\Gamma = 63.7\,\mathrm{m}^2/s$ for the 3 MW turbine and to $76.4\,\mathrm{m}^2/s$ for the 7 MW turbine (assuming $C_{T,WE}$ to be the same for both). It must be noted that the rotational speed as function of the wind speed is not revealed by the manufacturers and thus had to be estimated by the authors. Also, the $C_{T,WE}$ curve of the 7 MW turbine is unknown and therefore the same C_T as for the 3 MW turbine was used instead, leading to a circulation strength of $98.6\,\mathrm{m}^2/\mathrm{s}$.

The WE turbine wake-induced velocities are computed numerically at distances up to four WE rotor radii behind the turbine, and around distances centered at 500 m behind it. The wake is represented by eight revolutions of each blade's wake (beginning at the turbine in the first case, centered about the mean distance in the second case). Every revolution is discretized by 72 straight line vortex elements, each one representing a 5° increment. Induced velocities of these finite-length straight vortex elements, including a core radius model, are computed numerically.

The swirl velocity profile includes a core radius R_c, a lateral position within the rotor disk Y_0 and its swirl velocity magnitude depends on the vortex circulation strength Γ. Coordinates x, y, z and lengths such as the core radius and vortex location within the rotor disk are made non-dimensional by the helicopter rotor radius R, velocities are referred to the tip speed $U = \Omega R$ to provide the wake-induced inflow ratio λ_W as fraction of the helicopter tip speed. The circulation is made non-dimensional by division through UR. For an analytical solution of the problem sketched in Fig. 1 (c) the WE turbine vortex within the rotor disk is replaced by an equivalent infinitely long straight line vortex as sketched in Fig. 3.

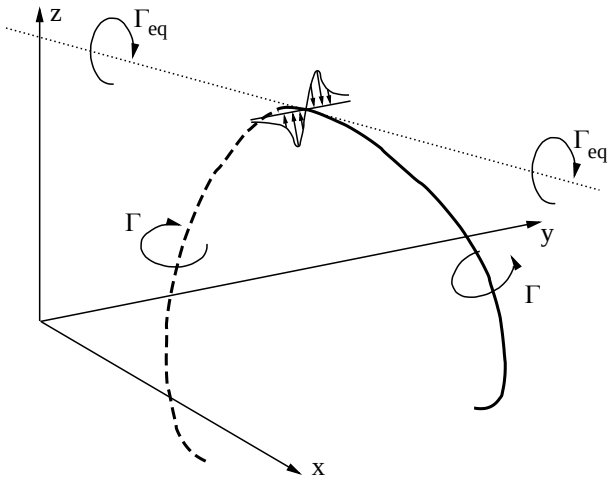

Fig. 3: Replacement of the WE rotor spiral vortex of strength Γ by an infinite long straight line vortex with strength Γ_{eq} to represent the vortex-induced velocity field in the upmost point.

This straight line vortex is modeled with a core radius model of Burnham-Hallock [10], which is a special case of the Vatistas' model [11]. The equivalent circulation Γ_{eq}, or the inflow ratio λ_{W0}, are then estimated based on the computed wake-induced velocity profiles. It turns out that for the cases investigated here this equivalent circulation is about half of the value of the WE spiral vortex strength.

$$\lambda_W = \frac{v_{iW}}{U} = \frac{\Gamma_{eq}}{2\pi U}\frac{y - Y_0}{\left(y - Y_0\right)^2 + R_c^{\,2}} = \lambda_{W0}\frac{r\sin\psi - y_0}{\left(r\sin\psi - y_0\right)^2 + r_c^{\,2}}; \quad \lambda_{W0} = \frac{\Gamma_{eq}}{2\pi UR} \tag{3}$$

The peak value of the inflow ratio is obtained at the core radius itself.

$$\lambda_{W,max} = \frac{\lambda_{W0}}{2r_c} = \frac{\Gamma_{eq}}{4\pi UR_c} \tag{4}$$

Natural diffusion is represented by time-dependent decay (or aging) functions for both the circulation strength (which reduces asymptotically to zero for long time) and the vortex core radius (which widens with time) in the following manner, following [10] and [12].

$$r_c = \frac{R_{c0}}{R}\sqrt{1 + \frac{5\cdot 10^{-6}\, rad/s}{\left(R_{c0}/R_{WE}\right)^2 \Omega_{WE}}\psi_v} \tag{5}$$

$$\Gamma = \Gamma_0 e^{-0.001932\psi_V}$$

The initial core radius R_{c0} is set to 5% of the WE chord length at 93% radius (i.e., the reference chord at the blade tip area). Both decay factors of the core

radius and the circulation aging functions are empirical, but based on measurements. These ‘’aging’’ functions of the tip vortex circulation and core radius are shown in Fig. 4. For the wind speed of 10 m/s investigated here 40 revolutions of the WE turbine account for a horizontal distance of 17.9 WE rotor diameters (= 2 km) downstream in case of the 3 MW turbine and 15.6 WE rotor diameters (= 2.4 km) in case of the 7 MW turbine. It can be seen that the vortex core radii range between 1% of the helicopter rotor radius shortly behind the WE turbine to about 40% far away from it.

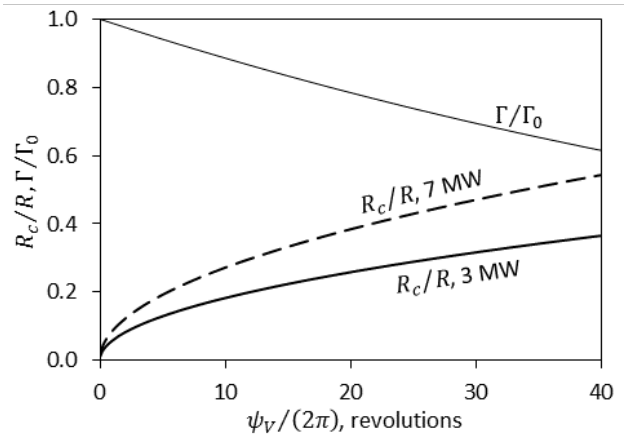

Fig. 4: Circulation and core radius aging functions.

For simplification the hypothesis is made that within the aircraft or helicopter rotor disk the vortex-induced velocity field does not change (i.e., an equivalent infinite long straight vortex is assumed). This is justified since the WE rotor radius is several times larger than the rotor radius. In case of the 3 MW turbine the WE-helicopter rotor ratio is 11.5 and in case of the 7 MW turbine it is 15.7. Therefore, the wake curvature within the rotor disk can be ignored.

Inflow ratio distributions that are computed based on Eq. (3) for arbitrarily chosen values of $r_c = 0.115$ (solid line) and larger core radii (2, 3, 4, 5 times the value, dashed lines) are shown in Fig. 5 (a) for a fixed core position $y_0 = 0.3$. In Fig. 5 (b) the vortex is centered in the hub and its core radius is larger than the rotor radius. It represents a cut through the rotor center in lateral direction and the WE vortex-induced velocity profile within it, having a lateral offset with respect to the rotor center as sketched in Fig. 1. In the first case Fig. 5 (a) the WE vortex-induced inflow profile is very non-linear, while in the second case (b) it is practically linear.

2.2. The fixed-wing aircraft model

For determination of vortex induced influences on an aircraft, the strip method has found widespread use as aerodynamic interaction model. It is based on lifting line theory and describes the additional aerodynamic forces and moments acting on an aircraft in

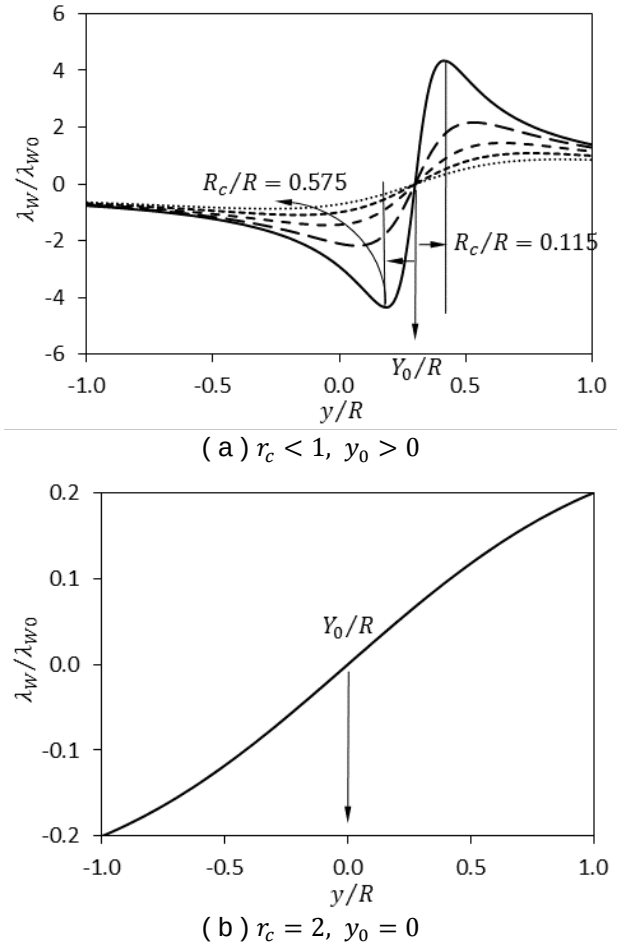

Fig. 5: Sketch of different possible induced velocity distributions across the rotor disk.

a spatial wind field, e.g. wake turbulence [1], [13], [14]. For computation of the forces and moments, the lift generating surfaces of the aircraft are subdivided into sections for which the vortex influence is determined. At each strip the additional angles of attack and angles of sideslip due to the local wind/vortices are computed. Using a suitable lift gradient, an additional lift is obtained for each strip. These local lift increments are weighted elliptically in span direction and then summarized, as well as the corresponding moments.

This method was validated against wind tunnel tests [15] and flight test data in [16] and [17]. The transversal flight of a fixed-wing aircraft into the tip vortex helix behind a wind energy rotor is considered to be a worst case scenario concerning yawing and rolling moment impact (Fig. 6). For a rotating-wing aircraft, any orientation of a vortex within the rotor will cause pitching and rolling moments. For an assumed flight path approximately parallel to the vortices axes, which is roughly in maximum and in minimum rotor tip altitude, the induced rolling moment is primarily of interest. Crossing the wake in shaft hub altitude, a yawing moment impact is dominating.

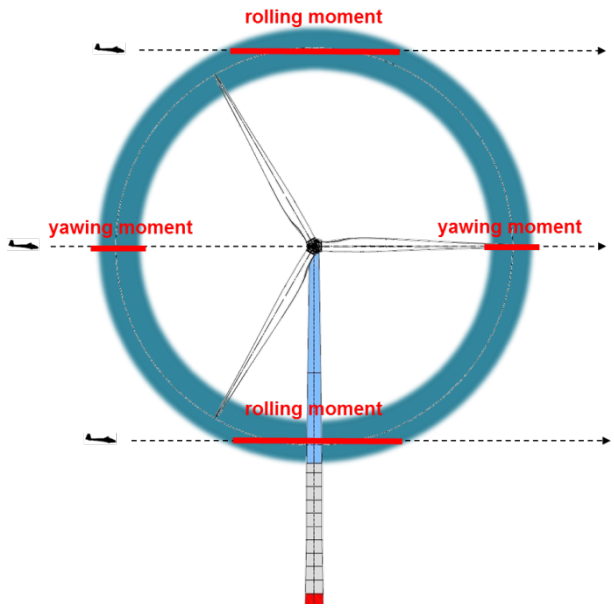

Fig. 6: Transversal flight into the rotor blade tip vortex behind a wind energy rotor.

Whereas the yawing moment influence is of short duration, the rolling moment impact is stronger and of longer duration – depending on the aircraft airspeed and encounter scenario. The rolling moment can be computed particularly well with the strip method.

The method is applied for two aircraft flying in the wind turbine rotor wake: Fig. 7 (a) a sailplane (Ka8-b) with 15 m wingspan and flying at the airspeed of $V = 17\,m/s$, and Fig. 7 (b) a helicopter with a rotor disk diameter of 10 m (Bo-105) and an airspeed of $V = 20\,m/s$.

For computation of the vertical forces and rolling moments generated by the local up- and downwind of the WE turbine wake vortices, the wing of the encountering aircraft is subdivided typically into 16 strips, see Fig. 7. The additional local angle of attack $\Delta\alpha_W$ induced by the local wake vertical wind $w_W(i)$ is determined at each strip i.

(6) $$\Delta\alpha_W(i) = \arctan\frac{w_W(i)}{V_\infty}$$

Then the additional local lift $\Delta C_L(i)$ is calculated at each strip with the overall aircraft lift gradient $C_{L\alpha}$.

(7) $$\Delta C_L(i) = C_{L\alpha}\Delta\alpha_W(i)\,f_W(i)$$

A weighting function $f_W(i)$ is applied assuming an elliptically lift distribution along the span b with the corresponding lever arms at each strip position $y(i)$.

(8) $$f_W(i) = \frac{4}{\pi}\sin\left(\arccos\frac{-2y(i)}{b}\right)$$

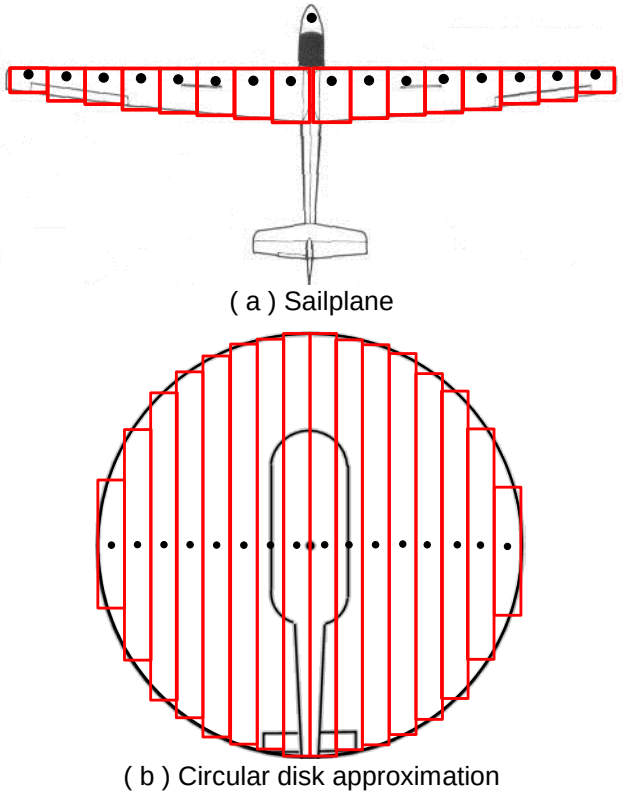

(a) Sailplane

(b) Circular disk approximation

Fig. 7: Strip method: wing discretization.

The effect on the rolling moment is computed with the respective lever arms as well and summed up for all strips. The applied overall aerodynamic lift gradients $C_{L\alpha}$ for the sailplane wing and the helicopter rotor disk are determined applying the Helmbold equation, depending on the aspect ratio Λ of the lift generating surface [18].

(9) $$C_{L\alpha} = 2\pi\frac{\Lambda}{2+\sqrt{4+\Lambda^2}}$$

The Helmbold equation is in between the Prandtl and the Barrows formulation and applicable for high aspect ratio wings as well as low aspect ratio tail surfaces or rotors [18]. The overall lift gradient is determined to (a) $C_{L\alpha} = 6$ for the sailplane with $\Lambda = 15.9$, and (b) $C_{L\alpha} = 1.83$ for the helicopter, represented by a circular disk with $\Lambda = 4/\pi = 1.273$.

2.3. The helicopter model

For flight mechanics purposes the Institute of Flight Systems at DLR uses the non-linear "Helicopter Overall Simulation Tool" HOST for desktop simulation [19]. HOST was developed by Airbus Helicopters and is now used and further developed in cooperation with ONERA and DLR. It is a modular tool that has the ability to simulate any type of helicopter and calculate trim, time domain response and perform linearization.

For the results obtained here HOST was used in a special configuration with the "Atmospheric Envi-

ronment Submodule". This submodule is connected to HOST's flight mechanics model, calculates disturbed air and provides all relevant helicopter parts with the related turbulence parameters. This is mainly the modified velocity due to the flow field of the vortex. An interaction which models the influence from rotor induced velocity to the vortex is not modelled. The Atmospheric Environment Module is able to simulate the following types of wake: atmospheric turbulence, big size aircraft vortex wake model, gusts in all directions, and the flow around different types of buildings.

All calculations performed here were conducted with the flight mechanics model of the BO105 helicopter and the so-called "Big Size Aircraft Vortex Wake Model". Therein, the vortices are described following the Lamb-Oseen formula [20], [21]. Its equivalent circulation strength or swirl velocity V_c, a core radius R_c and a decay factor β_V must be provided; they are estimated from the computed WE wake-induced velocity field. At a distance $y = 0$ from the core center this formula has a numerical singularity, but it can be proven that the analytical boundary value results in $v_W = 0$, because the expression in brackets of Eq. (10) approaches the zero faster than the division by y.

$$(10)\quad v_W = V_c \frac{R_c}{y}\left[1 - e^{-\beta_V\left(\frac{y}{R_c}\right)^2}\right];\quad V_c = \frac{\Gamma_{eq}}{2\pi R_c}$$

Note that for $y = R_c$ the resulting swirl velocity is $v_W = V_c\left(1 - e^{-\beta_V}\right)$ and for the value used of $\beta_V = 0.97$ the result is $v_W \approx 0.63V_c$. Also, the maximum swirl velocity is obtained at $y \approx 1.14R_c$, i.e. 14% larger than the specified value of R_c.

It is assumed that this wake model is able to represent the idealized vortex in the wake of a WE turbine while it is provided with the required vortex data core radius and swirl speed at the core radius. Because a trim calculation is used to investigate the effects of the wake vortex (represented by an equivalent airplane vortex) on the helicopter only the wake impact on the rotor is of interest. To achieve this no links between the wake model and helicopter parts other than the rotor are modelled. Due to the expected change in rotor thrust other changes to the aerodynamic helicopter parts are expected and should be visible in helicopter attitude.

The helicopter model used for these investigations, the Bo105, is a light utility rotorcraft and is used in maintenance of offshore wind farms. The model assumes an articulated rotor with rigid blades flapping about an effective hinge offset and the Meier-Drees model is used for the induced velocity calculation. It was configured with a mass of 2200 kg.

The purpose of the complete helicopter trim analysis is to compare the results with the analytical model estimates in order to investigate the differences between these two methods. For this comparison, the main rotor control angles dependent on the relative y-Positon from rotor to vortex center are used. For four scenarios A, B, C and D the helicopter reaction due to the vortex of a 3 MW or a 7 MW wind turbine in a distance of $y = 100\,m$ or $500\,m$ was computed. Therefore the HOST airplane wake model is provided with the data given in Table 2 for these cases.

Table 2: Properties of the HOST big size aircraft vortex wake model.

Scenario	WE	y, m	R_c, m	$V_c, m/s$
A	3 MW	100	0.393	10.5
B	3 MW	500	0.863	4.5
C	7 MW	100	0.542	12.0
D	7 MW	500	1.189	4.8

To determine the perturbation in main rotor control angles due to the aircraft vortex, the helicopter is trimmed with 10 km/h forward speed in the influence area of the vortex. The helicopter is positioned in a way that the vortex is in the same height as the rotor hub and is varied in position from $y = -2R$ to $+2R$ in steps of $0.25R$. The perturbation control angles are obtained by subtracting the trim controls of the undisturbed flow field without an aircraft vortex from the trim controls including the vortex.

2.4. The analytical rotor model

Based on the sketch of Fig. 1 (c) the velocities acting on a rotor blade element tangential (in the rotational plane, normal to the radial axis) and normal to the rotational plane can be established. It is assumed that the helicopter's flight path is parallel to the WE turbine's tip vortex axis, the vortex center lies in the plane of the rotor disk, and the rotor is horizontal. As indicated in the sketch the vortex center lies in the rotor disk and therefore only vertical vortex-induced velocities are acting on the blade elements. The vortex axis is assumed to be parallel to the rotor longitudinal x-axis and the vortex-induced velocities are a function of the lateral coordinate y only. All velocities can be split into those components present in an isolated rotor (index 0) and those components due to the WE wake λ_W from Eq. (3) that are considered as perturbations (Δ values).

$$(11)\quad \begin{aligned} V_T &= r + \mu\sin\psi \;\; = V_{T0} + \Delta V_T;\;\; \Delta V_T = 0 \\ V_P &= \mu_z + \lambda_i + \lambda_W = V_{P0} + \Delta V_P;\; \Delta V_P = \lambda_W \end{aligned}$$

A trim of the rotor requires collective and cyclic controls in order to establish the required thrust, propulsive and lateral forces, as well as the hub moments needed for a steady flight. Any perturbations of the

velocities acting at the blades therefore require perturbations in the controls in order to maintain the trim. Thus, the controls can be set up in a similar manner.

$$\begin{aligned}\Theta &= \Theta_0 + \Theta_S \sin\psi + \Theta_C \cos\psi \\ \Delta\Theta &= \Delta\Theta_0 + \Delta\Theta_S \sin\psi\end{aligned} \tag{12}$$

In a general case a $\Delta\Theta_C \cos\psi$ would be considered as well, but here a perturbation parallel to the x-axis is assumed (see Fig. 1 (c)) for simplification. This causes only lateral unbalance of disturbances while in longitudinal direction the disturbances are always balanced fore and aft of the rotor hub.

The blade section angle of attack is defined by three contributions: first, the pitch angle Θ, which is needed for the helicopter trim in undisturbed atmosphere. Second, a perturbation $\Delta\Theta$ (Eq. (12)) to compensate the trim disturbance caused by the third contribution, namely the WE vortex-induced velocities given in Eq. (11). These perturbation control angles are computed by the requirement of keeping the trim constant.

First, this results into an equation for the steady (mean) lift perturbation to be zero. Second, the $1/rev$ aerodynamic flapping moment perturbation about the hub must be zero as well. Both of these values require a radial integration of the section lift distribution from the effective begin of the airfoiled part of the blade A to the effective end of it B.

$$\begin{aligned}\Delta\overline{L} &= \int_A^B \Delta\overline{dL} \approx \int_A^B V_T^2 \left(\Delta\Theta - \frac{\Delta V_P}{V_T}\right) dr \\ &= \Delta\Theta_0 \int_A^B \left(r + \mu\sin\psi\right)^2 dr \\ &+ \Delta\Theta_S \int_A^B \left(r + \mu\sin\psi\right)^2 \sin\psi\, dr \\ &- \lambda_{W0} \int_A^B \frac{\left(r + \mu\sin\psi\right)\left(r\sin\psi - y_0\right)}{\left(r\sin\psi - y_0\right)^2 + {r_c}^2} dr\end{aligned} \tag{13}$$

The equation for the moment is:

$$\Delta\overline{M_\beta} = \int_A^B r\,\Delta\overline{dL} \tag{14}$$

The wake integral of the perturbation lift poses problems in analysis, since a Fourier series is needed for ease of further processing, but a broken rational function with periodic terms in both nominator and denominator is present. A Fourier analysis transforms this into the desired form.

$$\begin{aligned}&\int_A^B \left(r + \mu\sin\psi\right) \frac{r\sin\psi - y_0}{\left(r\sin\psi - y_0\right)^2 + {r_c}^2} dr \\ &= a_{W0} + \sum_{i=1}^{\infty} \left(a_{Wi}\cos i\psi + b_{Wi}\sin i\psi\right)\end{aligned} \tag{15}$$

We need the mean value a_{W0} for keeping the mean value of the lift perturbation zero ($\Delta\overline{L_0}$) and the $1/rev$ sine part b_{W1} for keeping the rotor roll moment perturbation zero (in the rotating frame that is $\Delta\overline{M_{\beta S}} = 0$), all higher harmonics are of no interest for the study here since they do not affect the rotor trim. A rotor pitch moment perturbation is not generated due to the vortex axis being parallel to the rotor y-axis (in the rotating frame: $\Delta\overline{M_{\beta C}} = 0$).

2.4.1. Approximate solution for $r_c \gg 1$, $y_0 = 0$

Let us first assume that the rotor is perfectly aligned with the vortex core center, i.e. $y_0 = 0$, and that the core radius of the WE vortex is larger than the helicopter rotor radius $r_c \gg 1$ as in Fig. 5 (b). In this case the helicopter rotor experiences only an approximately linear variation of vortex-induced velocities laterally across the disk with zero velocities in the center. Using Eq. (13) and inserting the linear form $\lambda_W = \lambda_{W0}\, y/R = \lambda_{W0} r\sin\psi$ leads to

$$\begin{aligned}0 &= \Delta\Theta_0 \int_A^B r^2 + \frac{\mu^2}{2} dr \\ &+ \Delta\Theta_S \int_A^B \mu r\, dr - \lambda_{W0} \int_A^B \frac{\mu r}{2} dr \\ &= \Delta\Theta_0 \left(2c_3 + \mu^2 c_1\right) + \Delta\Theta_S \mu 2c_2 - \lambda_{W0}\mu c_2 \\ &= \Delta\Theta_0 d_0 + \Delta\Theta_S d_S - \lambda_{W0} d_W \\ c_i &= \int_A^B r^{i-1} dr = \frac{B^i - A^i}{i}\end{aligned} \tag{16}$$

The application of the linear WE inflow variation to Eq. (14) leads to the second equation to determine the collective and cyclic perturbation controls.

$$\begin{aligned}0 &= \Delta\Theta_0 \int_A^B 2\mu r^2\, dr \\ &+ \Delta\Theta_S \int_A^B r^3 + \frac{3\mu^2}{4} r\, dr - \lambda_{W0} \int_A^B r^3\, dr \\ &= \Delta\Theta_0 \mu^2 8c_3 + \Delta\Theta_S \left(4c_4 + 3\mu^2 c_2\right) - \lambda_{W0} 4c_4 \\ &= \Delta\Theta_0 e_0 + \Delta\Theta_S e_S - \lambda_{W0} e_W\end{aligned} \tag{17}$$

Now Eqs. (16) and (17) can easily be combined to solve for $\Delta\Theta_0$ and $\Delta\Theta_S$.

$$\Delta\Theta_S = \lambda_{W0}\frac{d_W e_0 - e_W d_0}{d_S e_0 - e_S d_0}$$

(18)

$$\Delta\Theta_0 = \frac{\lambda_{W0} d_W - \Delta\Theta_S d_S}{d_0} = \frac{\lambda_{W0} e_W - \Delta\Theta_S e_S}{e_0}$$

An interesting result is obtained for the case $A = 0$, $B = 1$ and in hovering condition where $\mu = 0$:

(19) $$\Delta\Theta_S = \lambda_{W0} \quad \text{and} \quad \Delta\Theta_0 = 0$$

2.4.2. Exact solution for $r_c \gg 1$, $y_0 = 0$

Following the derivation given in the appendix the coefficients a_{W0} and b_{W1} can be computed and the expressions equivalent to Eqs. (16) and (17) evaluated. The result is of course more involved. For the lift equation it is

$$\begin{aligned} 0 &= \Delta\Theta_0\left(2c_3 + \mu^2 c_1\right) + \Delta\Theta_S \mu 2c_2 \\ &\quad - \lambda_{W0}\mu \ln\left(1 + \sqrt{1 + \left(r/r_c\right)^2}\right)\Big|_A^B \\ &= \Delta\Theta_0 d_0 + \Delta\Theta_S d_S - \lambda_{W0} d_W \end{aligned} \tag{20}$$

For the moment equation it is

$$\begin{aligned} 0 &= \Delta\Theta_0 8\mu^2 c_3 + \Delta\Theta_S\left(4c_4 + 3\mu^2 c_2\right) \\ &\quad - \lambda_{W0} 2\left[c_2 - r_c^{\,2}\sqrt{1 + \left(r/r_c\right)^2}\Big|_A^B\right] \\ &= \Delta\Theta_0 e_0 + \Delta\Theta_S e_S - \lambda_{W0} e_W \end{aligned} \tag{21}$$

To compute the perturbation angles of attack, Eq. (18) is used again.

2.4.3. Exact solution for arbitrary core radius and lateral vortex position

The most general solution of Eq. (13) is mathematically very involved and the full derivation is given in the appendix. Here only the results of the wake integrals in Eqs. (13) and (14) are given. To simplify the expressions of the results the following abbreviations are used.

(22) $$\xi = r^2 - |y_0|^2 + |r_c|^2 \qquad \eta = 2|y_0||r_c|$$

Then the wake integral of the lift equation becomes

(23) $$d_w = \int_A^B a_{W0}\, dr$$

With the derivation given in the appendix this becomes

$$\begin{aligned} d_w &= \mu \ln\sqrt{\sqrt{\xi^2 + \eta^2} + \xi + 2y_0^{\,2}}\Big|_A^B \\ &\quad + \mu \ln\left(1 + \frac{\sqrt{2}|r_c|}{\sqrt{\sqrt{\xi^2 + \eta^2} + \xi}}\right)\Big|_A^B \\ &\quad + y_0 \frac{\sqrt{2}|r_c|}{\sqrt{\sqrt{\xi^2 + \eta^2} + \xi}}\Big|_A^B \end{aligned} \tag{24}$$

and that of the moment equation becomes

$$\begin{aligned} e_W &= \int_A^B r b_{W1}\, dr \\ &= c_2 + 2\mu y_0 \ln\sqrt{\sqrt{\xi^2 + \eta^2} + \xi + 2y_0^{\,2}}\Big|_A^B \\ &\quad + 2\mu y_0 \ln\left(1 + \frac{\sqrt{2}|r_c|}{\sqrt{\sqrt{\xi^2 + \eta^2} + \xi}}\right)\Big|_A^B \\ &\quad + 2\mu\,\mathrm{sgn}(y_0)|r_c| \arctan\frac{\sqrt{2}|y_0|}{\sqrt{\sqrt{\xi^2 + \eta^2} + \xi}}\Big|_A^B \\ &\quad - \sqrt{2}|r_c|\sqrt{\sqrt{\xi^2 + \eta^2} + \xi}\Big|_A^B \\ &\quad + \sqrt{2}|y_0|\sqrt{\sqrt{\xi^2 + \eta^2} - \xi}\Big|_A^B \end{aligned} \tag{25}$$

To compute the perturbation angles of attack, Eq. (18) is used again.

3. RESULTS

3.1. Wake-induced velocity fields

In order to get a feeling for the magnitude of WE turbine tip vortex induced velocities with respect to the helicopter rotor blade tip speed the vortex circulation is non-dimensionalized by ΩR^2 of the helicopter. This provides the order of magnitude of peak inflow ratio velocities with results shown for the values of circulation given in Sect. 2.1. The parameters needed are summarized in Table 3.

At practical distances of 100-500 m to the WE turbine the core radius growth leads already to a significant reduction of peak vortex induced velocities (shown later) that are in the range of the hovering rotor mean thrust-induced inflow ratio $\lambda_{i0} = \sqrt{C_T/2} = 0.0506$, which is representative of a 2.3 ton Bo105 helicopter with a thrust coefficient of $C_T = 0.00512$.

Table 3: Circulation and peak induced inflow ratio.

WE turbine	3 MW	7 MW
Γ, m²/s (Eq. (2))	63.7	98.6
Γ_{eq}, m²/s (Eq. (3))	31.9	49.3
λ_{W0} (Eq. (3), $\psi_V = 0°$)	0.00474	0.00733
λ_{W0} $(y = 100m)$	0.00453	0.00704
λ_{W0} $(y = 500m)$	0.00400	0.00629
r_{c0} $(\psi_V = 0°)$	0.0102	0.0138
r_{c0} $(y = 100m)$	0.080	0.110
r_{c0} $(y = 500m)$	0.177	0.242
$\lambda_{W,max}$ (Eq. (4), $\psi_V = 0°$)	0.233	0.266
$\lambda_{W,max}$ $(y = 100m)$	0.0283	0.0320
$\lambda_{W,max}$ $(y = 500m)$	0.0113	0.0130

The peak inflow ratio at the vortex core radius is shown in Fig. 8. Instead of the time development as shown in Fig. 4 here the development is given in terms of the distance downstream the WE turbine, beginning with one rotor diameter behind the WE blade tip, i.e., the helicopter would have a clearance of only one rotor radius. Initially, the peak WE vortex-induced inflow ratios even exceed the hovering helicopter's mean induced inflow value, but with increasing distance to the WE turbine they continuously decrease, following Eq. (5).

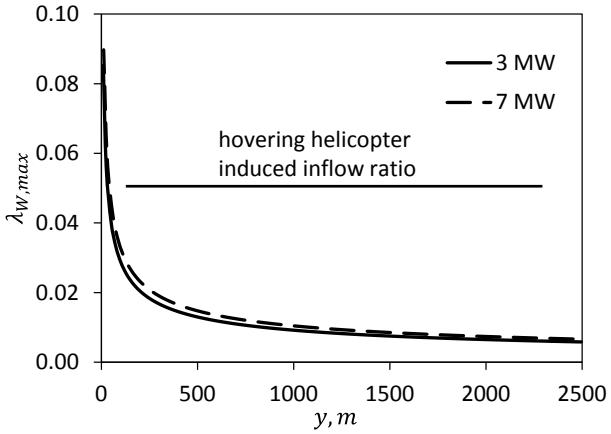

Fig. 8: WE vortex-induced peak inflow ratio.

For evaluation of the WE wake-induced velocities effect on rotor trim and the amount of trim controls needed for disturbance rejection, the induced velocity field at various distances to the WE turbine need to be computed. The velocity profiles at the top centerline of the wake spiral are given in Fig. 9 (a) around a short distance to the turbine of 120 m and around a longer distance of 500 m in (b). The helicopter's size is sketched in the middle of the graph in order to provide the size of its rotor with respect to the spacing of the WE vortices.

It is evident that at this wind speed of maximum circulation strength the vortex separation is always larger than the helicopter rotor diameter. These velocity data have been evaluated with a spatial resolution of 0.5 m in all directions. At young vortex ages, in the left half of Fig. 9 (a), some peak values of the 3 MW data are missed due to this resolution because the vortex core radii are smaller than the data resolution. However, within the rotor disk diameter of 9.82 m usually 19 samples are covered which is thought of as sufficient for the evaluation of the integral effect on the aerodynamic roll moment.

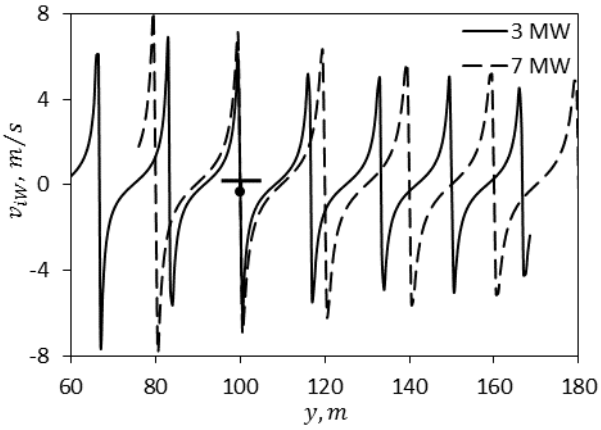

(a) Short distance around 120 m

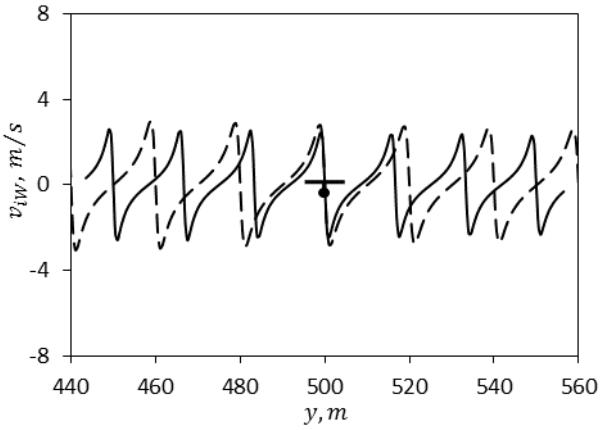

(b) Medium distance around 500 m

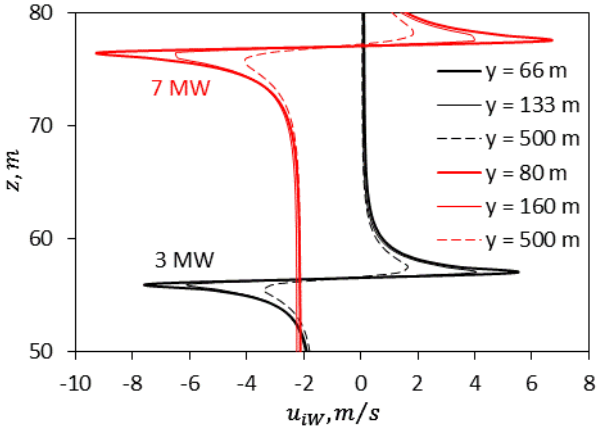

(c) Horizontal velocity profile at various distances

Fig. 9: WE vortex-induced velocity profiles at various distances behind the WE turbine.

Fig. 9 (c) shows the horizontal WE vortex-induced velocities along the vertical axis through a vortex center at different distances to the turbine. In all cases the 7 MW turbine's velocities are larger than those of the 3 MW turbine, but the core radii are larger and the vortex spacing is larger as well.

3.2. Fixed-wing aircraft roll control ratio

In order to assess the potential severity of the wake impact on the encountering aircraft the induced rolling moment $C_{l,W}$ is related to the controllability of the encountering aircraft applying the maximum roll control power $C_l(\delta_{a,max})$ [22], [23]. This relation defines the dimensionless vortex induced Roll Control Ratio RCR.

$$\mathrm{RCR} = \left| \frac{C_{l,W}}{C_l\left(\delta_{a,\max}\right)} \right| \qquad (\textit{fixed wing}) \tag{26}$$

$$\mathrm{RCR} = \left| \frac{C_{l,W}}{C_l\left(\Theta_{\mathrm{S,max}}\right)} \right| \qquad (\textit{rotorcraft})$$

The maximum roll control power of the sailplane is assumed to $|C_l(\delta_{a,max})| = 0.1$, based on available data for corresponding aircraft types [24]. The maximum helicopter roll control power is based on the assumption of an authority of $2500\,Nm/deg$ with a maximum longitudinal cyclic pitch angle of $\Delta\Theta_{S,max} = 8\,deg$. It is thus determined for the equivalent circular disk wing at a flight speed of 20 m/s as $|C_l(\Delta\Theta_{S,max})| = 0.22$, which is more than twice as high as for the sailplane. This is due to the fact that the sailplane aileron has a long lever arm, but only a relatively small control surface, while the helicopter uses the entire rotor blade as control surface.

Fig. 10 shows the magnitude of the roll control ratio of the Ka8-b sailplane with 15 m wing span and a helicopter with 10 m rotor disk diameter flying transversal 100 m behind the wind turbine across the upper part of the wake.

The results shown in Fig. 10 (a) indicate that a considerable rolling moment is imposed on the sailplane around the tip vortex position and between successive vortices. Regions with RCR > 100% are observed, in which the rolling moment imposed from the WE turbine wake vortices *cannot* be compensated by the ailerons. The hazards during flight in a vortex center or in between vortices are in the same magnitude, but in opposite rotational direction. Shape and magnitude of the hazard zones depend not only on blade circulation and rotational speed, but also on aircraft wing span and wind speed.

For the helicopter (10 m rotor diameter) flying at 20 m/s airspeed the situation is different (Fig. 10 (b)): the maximum roll control ratio never exceeds RCR = 0.22 in the wake of a 3 MW turbine at 10 m/s wind speed. This is rated as fully controllable. Moreover, noticeable rolling moments are only imposed at a flight into the center of a vortex, not in between two successive ones (as for the sailplane). The main reasons for this are higher roll control power of the helicopter and less influence to disturbances.

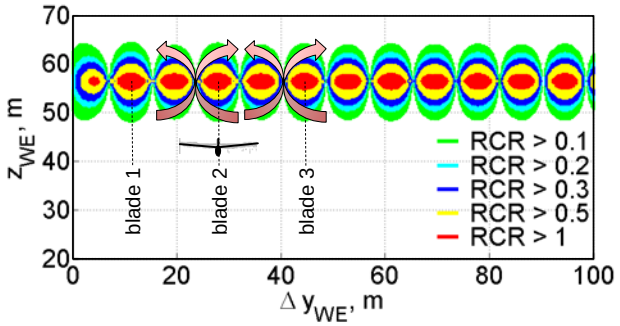

(a) Sailplane with 15 m wing span

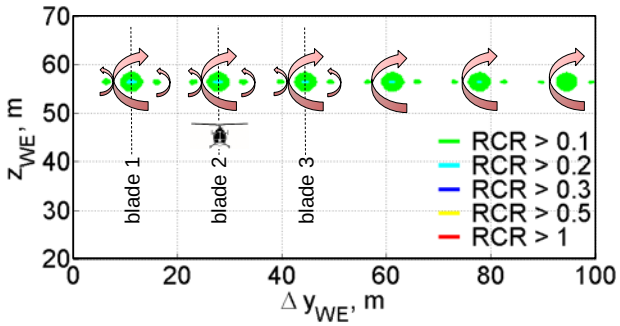

(b) Helicopter with 10 m rotor disk diameter

Fig. 10: Distribution of RCR magnitude of a sailplane and a helicopter (figure center 100 m behind a 3 MW wind energy turbine), $V_W = 10\ \mathrm{m/s}$.

Fig. 11 shows the RCR results for a transversal helicopter flight 100 m behind a 7 MW wind turbine at 10 m/s wind speed. The WE turbine rotor radius is 77 m, and the maximum roll control ratio is now RCR = 0.33. This is also rated as fully controllable.

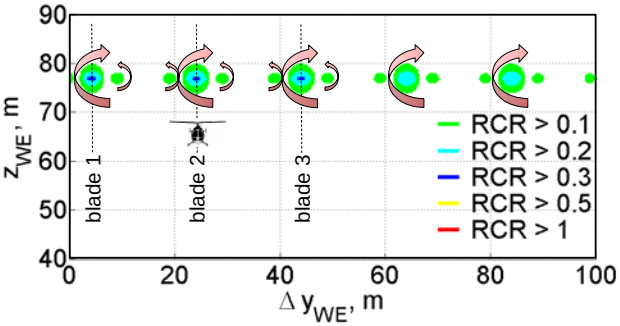

Fig. 11: Distribution of RCR magnitude of a helicopter (figure center 100 m behind a 7 MW wind energy turbine), $V_W = 10\ \mathrm{m/s}$.

3.3. Impact on helicopter trim

The following results were calculated with the helicopter model described in Section 2.3. Fig. 12 dis-

plays the total induced velocity distribution within the rotor disk for scenario A of Table 2, including the disturbance due to a wing tip vortex. In this example the vortex is located at the same height as the hub but $0.5\mathrm{R}$ left of the hub center. Positive values denote downwash, thus the vortex is rotating clockwise when seen from behind with upwash on the left and downwash on the right of its axis. The fundamental induced velocity distribution represents a small longitudinal gradient due to the small flight speed, but the lateral gradient is very small, following the Meijer-Drees model. The vortex axis could not be made fully parallel to the rotor x-axis and has a remaining 5° orientation misalignment, thus generating a slight aerodynamic pitch moment as well.

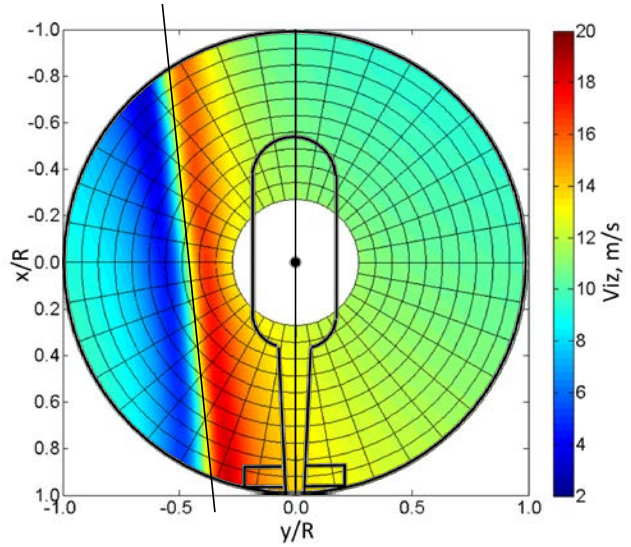

Fig. 12: Induced velocity distribution within the rotor disk, $\mu = 0.0127, C_T = 0.0049$.

Fig. 13 shows the perturbations of the main rotor trim control angles caused by the equivalent airplane blade tip vortex, dependent on the y-position of vortex core relative to the rotor hub, for each scenario of Table 2. The vortex location relative to the rotor hub ranges from $y_0 = -2$ to $+2$, i.e. from the far left side to the far right side.

Fig. 13 (a) shows the collective rotor control angle perturbation. When the vortex is in the left half of the rotor ($y_0 < 0$) more collective is needed to compensate the vortex induced downwash that dominates over the rotor disk. When the vortex core is at the rotor hub ($y_0 = 0$) the collective control angle is nearly zero because the downwash on the left side equals the upwash on the right side. When the vortex is on the right side of the rotor less collective is needed because the vortex-induced upwash dominates over the rotor disk.

Comparing the graphs of the four scenarios the 7 MW turbine causes a larger perturbation in control angle than the 3 MW turbine. Also, the closer the distances to the turbine, the larger the control perturbation. This is obvious because the vortex core swirl speed has the largest values for these conditions.

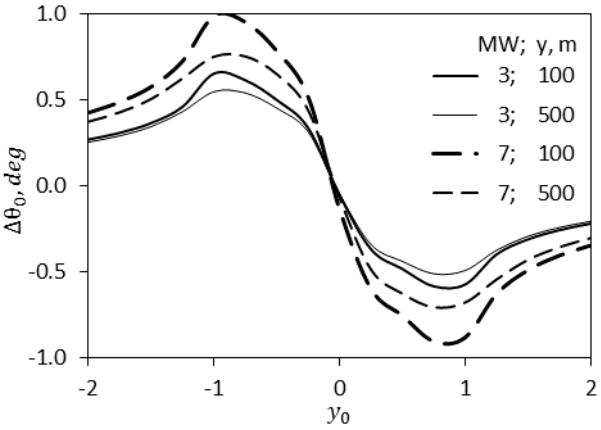

(a) Collective control

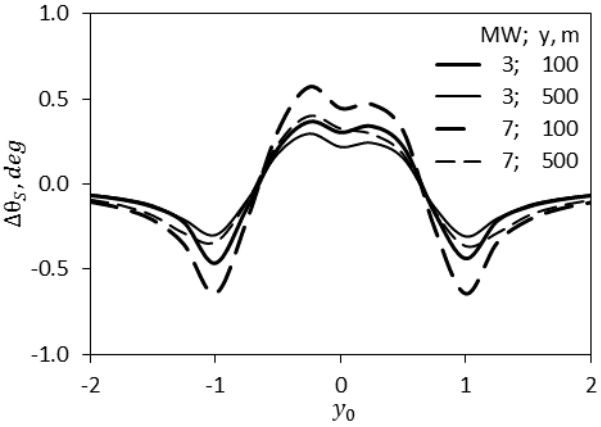

(b) Longitudinal control

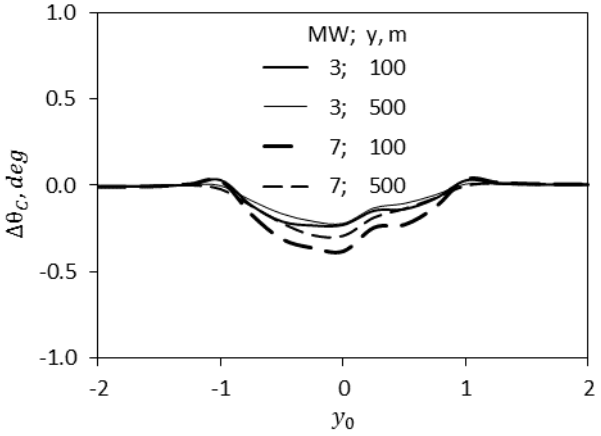

(c) Lateral control

Fig. 13: WE vortex impact on helicopter flight trim, μ = 0.0127, $A = 0.25$, $B = 0.97$.

Fig. 13 (b) displays the perturbations of the longitudinal rotor control angle $\Delta\theta_S$. Due to the vortex orientation relative to the rotor it was expected that aerodynamic roll moments will appear causing changes in the longitudinal control angle to cancel the vortex impact on trim. The plot shows the biggest changes

when the vortex is located at $y_0 = -1$, 0 and +1. When the vortex core is at the rotor hub ($y_0 = 0$) it causes as much downwash on the right side of the rotor as upwash on the left side. A positive aerodynamic roll moment appears and needs to be compensated by a positive longitudinal control angle. The vortex effect on the aerodynamic rotor roll moment becomes zero for the positions $y_0 = \pm 0.63$, which means that the downwash on the right side of the vortex and the upwash on the left are compensating each other with respect to the aerodynamic rotor roll moment.

When the vortex is located at either end of the rotor disk the longitudinal control needed to compensate its influence is negative in both cases. This is due to the vortex-induced velocity gradients within the rotor disk. For $y_0 = -1$ the entire disk is immersed in downwash of the vortex, with largest values on the left side of the disk, thus a positive gradient from left to right. For $y_0 = +1$ the entire disk is immersed in upwash of the vortex, with largest values on the right side of the disk, thus again a positive gradient from left to right. Therefore, in both cases a negative longitudinal control is needed to compensate this gradient.

Finally, Fig. 13 (c) displays the perturbations of the lateral control angle $\Delta\theta_C$. From simple theory no perturbations are expected, since the vortex does not introduce a longitudinal gradient of velocities within the rotor disk. However, generally a perturbation appears with largest values between $y_0 = -1$ and +0.5 (due to vortex misalignment and overall helicopter trim). All controls shown in Fig. 13 that are required to compensate the WE turbine wake vortex effects are small to moderate, compared to an available control bandwidth of approximately 8 deg.

As described in the technical approach the complete helicopter is simulated and not only the isolated rotor. Although no vortex effects on helicopter parts different from the rotor are considered the change in rotor thrust distribution and therefore its torque may cause a different tail rotor thrust. This represents a lateral force acting on the helicopter that has to be compensated by an associated lateral force of the main rotor for a trimmed flight. Due to the tail rotor position this change in tail rotor thrust will also cause a roll moment of the helicopter that the main rotor also has to compensate. Altogether, this leads to different helicopter pitch attitudes and roll angles, which in return will affect the other helicopter parts and finally will have an influence also on the lateral rotor control angle.

To confirm this hypothesis the helicopter pitch and roll angle perturbations relative to the trim without the WE vortex are shown in Fig. 14. The fuselage pitch angle (a) correlates with the lateral control angle perturbations of Fig. 13 (c) and the roll angle in Fig. 14 (b) correlates to the collective control in Fig. 13 (a). Although this is no proof of the entire physical chain of events as outlined before, it is an indicator that the entire helicopter trim is modified by the vortex influence on the main rotor only.

In addition, the Bo105 is a hingeless rotor system with a relatively large equivalent flapping hinge, leading to a phase delay between control input to flapping reaction of roughly 78° (a central hinge as assumed in the analytical estimate has a delay of 90°). Therefore, a trim about the pitch axis mainly requires longitudinal control, but also a part of lateral control.

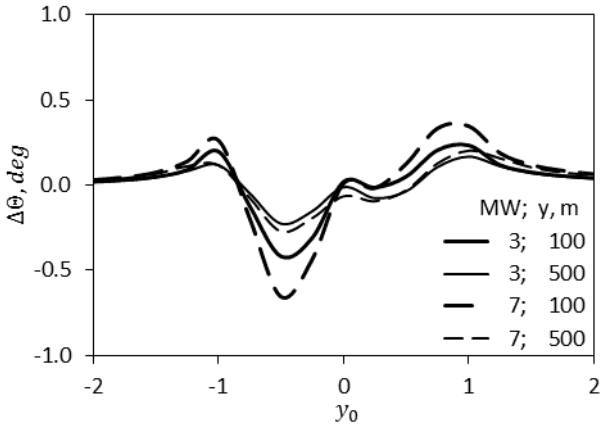

(a) Pitch attitude perturbations

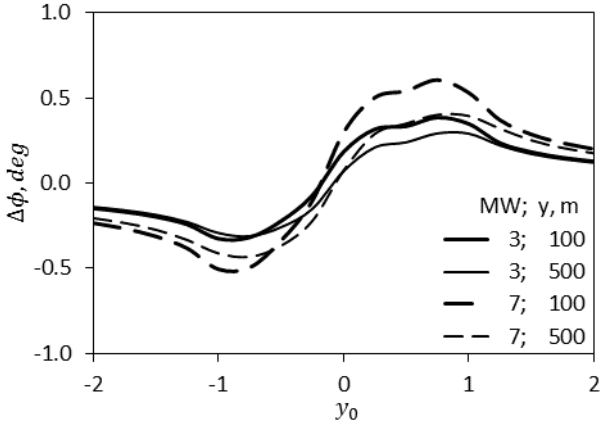

(b) Roll angle perturbations

Fig. 14: Helicopter pitch and roll angle perturbations due to a WE vortex.

3.4. Analytical estimation of rotor controls

First, the different velocity profiles resulting from different core radii are shown in Fig. 15 (a) and in (b) the variation of WE vortex induced velocities for varying vortex position within the rotor disk is shown for $r_c = 0.5$.

It is obvious that for small core radii a large non-linear impact on the rotor blade aerodynamics is present and only for core radii much larger than the rotor radius the velocity profile becomes practically

linear. Realistic WE vortex core radii will be a fraction of the rotor radius and then the vortex position within the rotor disk combines with the non-linearity of the velocity profile as seen in (b). The largest impact on rotor cyclic control is expected from these velocity profiles for the central WE vortex position where upwash is on the entire left rotor side and downwash on the entire right side, and also for the cases when the WE vortex is centered at the rotor radius when the WE induced velocity gradients across the disk appear largest.

The effect of the WE vortex lateral position within the rotor disk on longitudinal and collective control is shown in Fig. 16 (a) and (b) for different vortex core radii. Both trim control perturbations are linearly proportional to λ_{W0} and therefore the ratio $\Delta\Theta/\lambda_{W0}$ is independent of it; the magnitude of the controls is obtained when multiplying by the values actually encountered as given in Table 3.

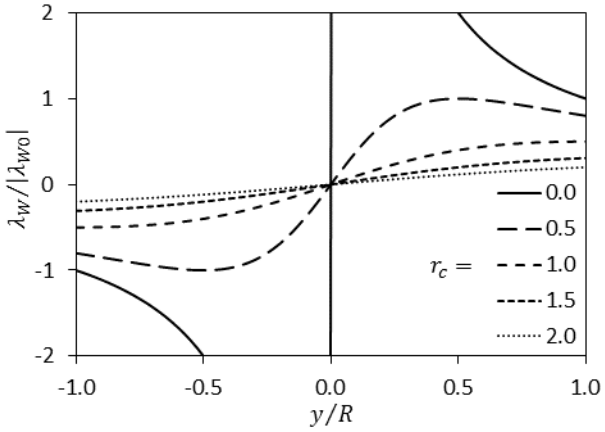

(a) Influence of vortex core radius, $y_0 = 0$

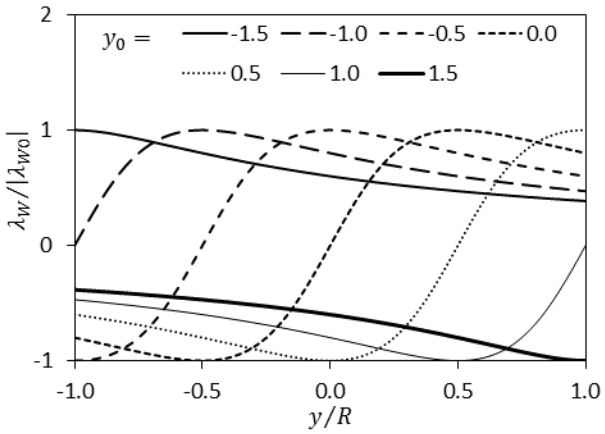

(b) Influence of vortex position, $r_c = 0.5$

Fig. 15: WE vortex induced velocity profiles within the rotor disk.

A potential vortex with a step jump from infinite upwash to infinite downwash in its center is represented by $r_c = 0$, while realistic WE core radii are more in the range up to $r_c = 0.1 - 0.5$, depending on their age, see Table 3.

When the vortex center is to the left outside the rotor disk, $y_0 = -2$, the entire rotor is immersed in the downwash side with diminishing magnitude towards the starboard (advancing) side. Therefore, the mean value is downwash with a gradient from left to right. This mean value requires a small positive collective (Fig. 16 (b)) to compensate the loss of thrust. The opposite is the case for a vortex position to the right outside the rotor disk, $y_0 = 2$. For $y_0 = -2$ the lateral gradient with more downwash of the vortex-induced velocities on the left side of the disk than on the right requires a small negative longitudinal cyclic (Fig. 16 (a)) to compensate the aerodynamic moment. The flat lines in the center area of the curves for $r_c = 0$ are due to the root cutout of $A = 0.25$.

When the vortex core reaches the left end of the rotor disk, $y_0 = -1$, the maximum values of mean downwash and downwash gradients are obtained within the rotor, thus the largest amount of collective and cyclic are needed to compensate for the loss of lift and the large aerodynamic moments developing. The opposite is the case for a vortex position to the right outside the rotor disk, $y_0 = 1$.

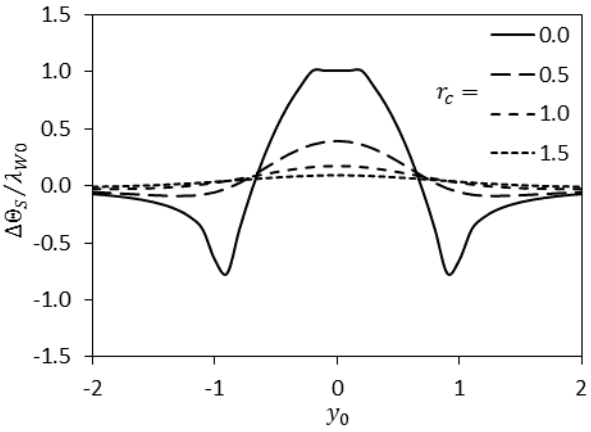

(a) Longitudinal cyclic

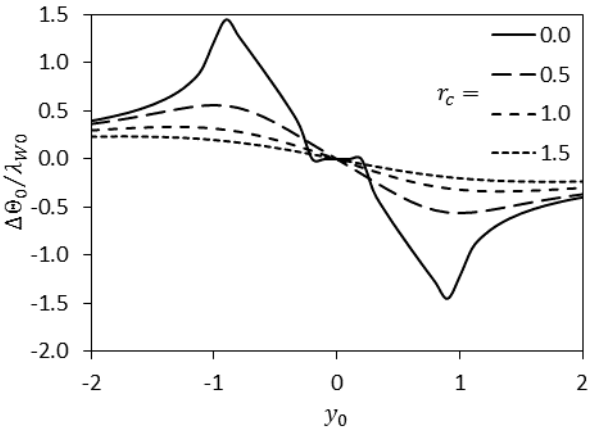

(b) Collective control

Fig. 16: Exact solution of the interactional problem for a WE turbine wake vortex, $A = 0.25$, $B = 0.97$.

Any position of the WE vortex inside the disk combines downwash on its right side with upwash on its left until the center position $y_0 = 0$ is a perfect balance of both. In this case no collective is needed because the mean inflow is zero due to this balance. However, this represents the largest aerodynamic moment induced by the WE vortex and thus the largest cyclic control is needed in this case to counteract this moment.

A comparison with the complete helicopter flight trim results as shown in Sect. 3.3 with the analytical results are given in Fig. 17. The advance ratio in both cases is $\mu = 0.0127$, the peak collective control values are taken as mean value of the extremes and the longitudinal control angles are taken from the vortex middle position at $y_0 = 0$. Although the trend appears to be quite similar as already seen in Fig. 13 (a) and (b) the absolute values of the flight trim are larger by roughly a factor of 2.

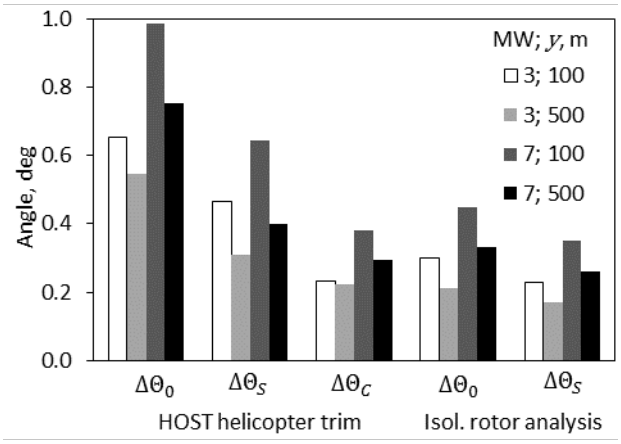

Fig. 17: Comparison of HOST complete helicopter trim perturbations with isolated rotor analysis, μ = 0.0127, $A = 0.25$, $B = 0.97$.

A reason for these differences is seen in the modified trim of the entire helicopter. Any inclusion of the WE vortex modifies the main rotor torque that has to be compensated by the tail rotor with additional thrust, leading to a lateral force and a roll moment which both the main rotor has to compensate. This leads to different pitch and roll attitude of the entire helicopter which in reverse affects the cyclic and collective pitch of the main rotor blades. However, the trend is captured correctly by the analytical model.

The influence of the advance ratio μ is given next in Fig. 18 for the same variations of vortex position and core radius. Mainly the increase of dynamic pressure on the advancing (starboard) side of the rotor dominates over the loss of dynamic pressure on the retreating side.

With increasing μ the resulting curves of cyclic and collective control become non-symmetric and the control magnitudes are larger when the vortex is located on the advancing side. Finally, the influence of the aerodynamically effective blade area can be analyzed.

So far, the parameters for a realistic rotor blade were used, i.e., an effective non-dimensional begin of the airfoiled part of the blade at $A = 0.25$ and an effective blade tip at $B = 0.97$. In Fig. 19 (a) and (b) a rotor blade beginning in the rotor center $A = 0$ and ending at the true radius $B = 1$ is shown for comparison with the former results and (c) and (d) give results obtained with $A = 0.5$ and $B = 0.97$.

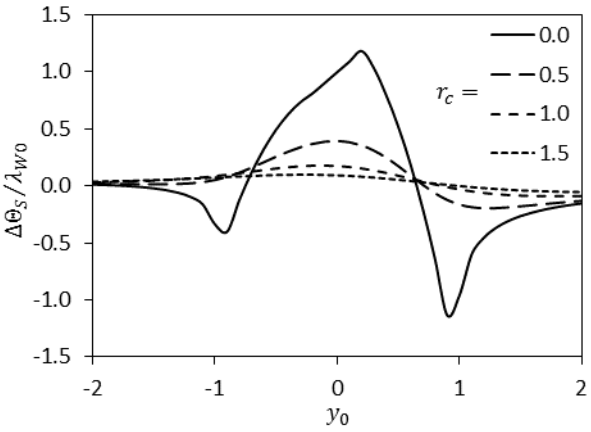

(a) Longitudinal cyclic, $\mu = 0.3$

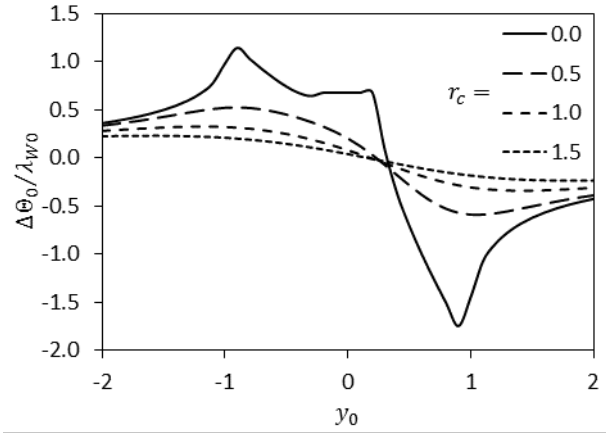

(b) Collective control, $\mu = 0.3$

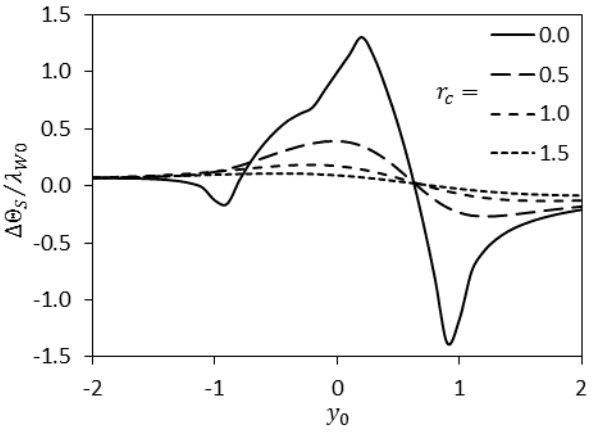

(c) Longitudinal cyclic, $\mu = 0.5$

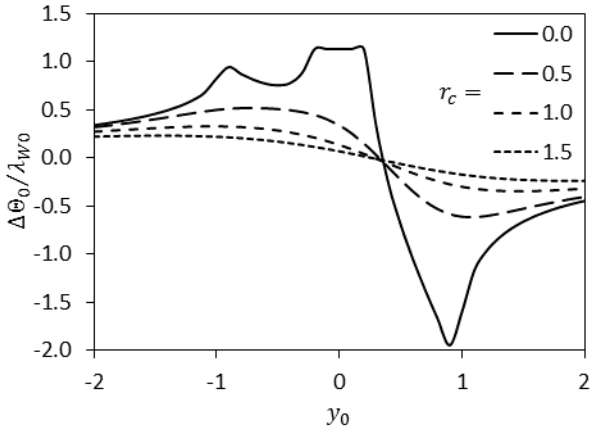

(d) Collective control, $\mu = 0.5$

Fig. 18: Influence of the advance ratio on the interactional problem, $A = 0.25$, $B = 0.97$.

Mainly the root cutout dominates the magnitude of collective and cyclic control needed. This is especially the case for small vortex core radii and vortex positions around the rotor center. In that case the root cutout effectively eliminates the vortex influence in this area. For core radii larger than the root cutout there is no practical difference to the results shown before in Fig. 16.

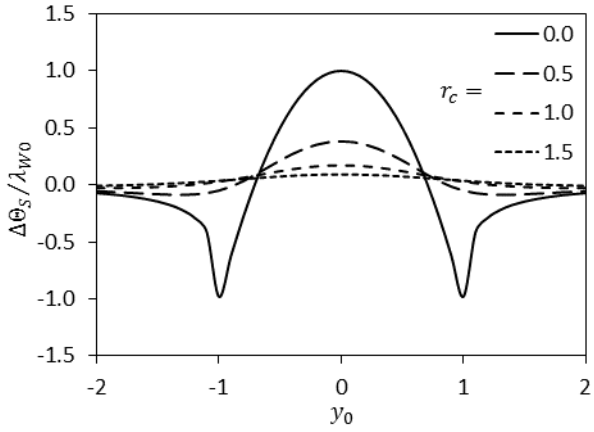

(a) Longitudinal cyclic, $A = 0, B = 1$

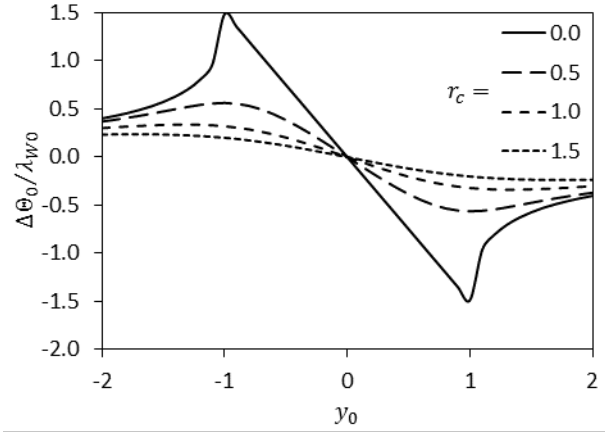

(b) Collective control, $A = 0, B = 1$

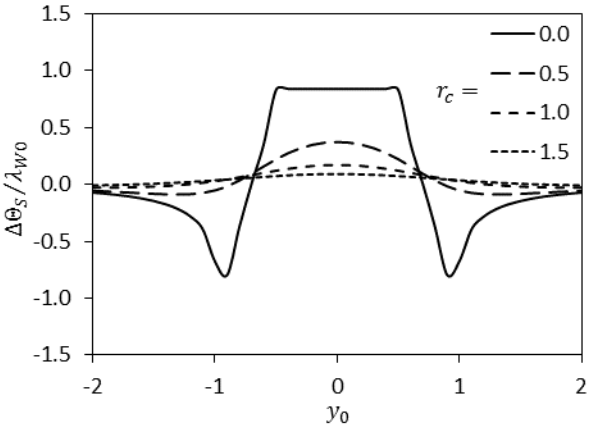

(c) Longitudinal cyclic, $A = 0.5, B = 0.97$

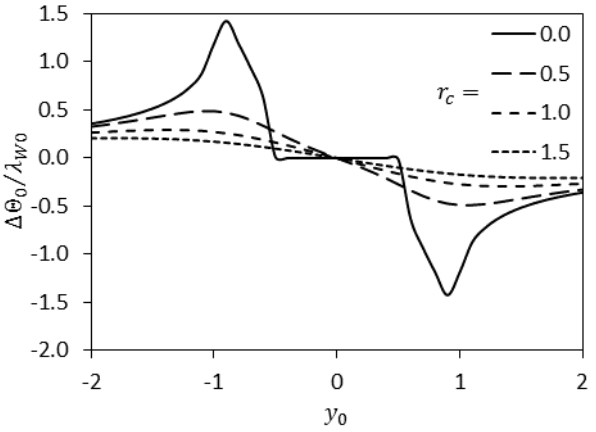

(d) Collective control, $A = 0.5, B = 0.97$

Fig. 19: Influence of the effective blade length on the interactional problem, $\mu = 0$.

4. COMPARISON OF RCR RESULTS

Assuming a control margin of $\Delta\Theta_{max} = 8°$ available (this is arbitrary to some degree and may be different for any individual helicopter) for compensating WE vortex-induced perturbations the peak values of Fig. 13 can be used to compute a roll control ratio RCR. The roll control ratio can here be defined as the combination of the perturbations in collective and cyclic controls, referenced to the maximum available control margin:

$$RCR = \frac{\left|\Delta\theta_0\right| + \sqrt{\Delta\Theta_S^2 + \Delta\Theta_C^2}}{\Delta\Theta_{max}} \tag{27}$$

This can be compared with the RCRs of Fig. 10 and Fig. 11 for the helicopter treated as a fixed-wing circular disk, and to the RCR computed from the perturbations of the simple analytical isolated rotor model given in Fig. 17. The result is given in Fig. 20 (a) for the variation of WE vortex position relative to the hub center, based on the data shown in Fig. 13. The largest combined collective and cyclic perturbations are needed when the vortex center is located at the right or left end of the rotor disk. This is be-

cause of the relatively large collective required at these vortex positions, leading to the entire rotor being exposed to the vortex downwash or upwash, depending on its position at the right or left end of the disk. This also generates the largest lateral induced velocity gradient across the disk, and thus the largest longitudinal cyclic control $\Delta\Theta_S$ to compensate it.

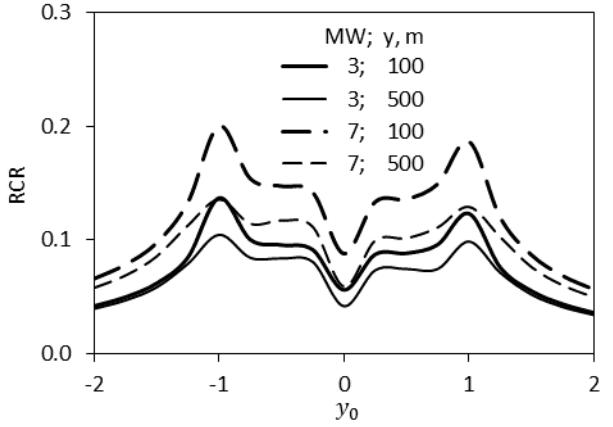

(a) Roll control ratio computed from Fig. 13

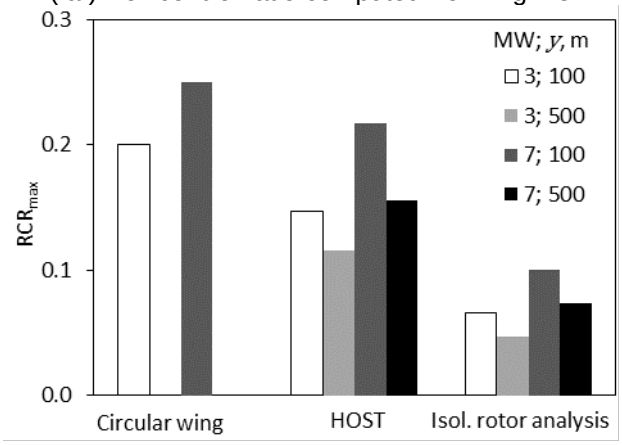

(b) Maximum roll control ratios for the different methods of analysis

Fig. 20: Roll control ratio comparison of Bo105 helicopter trim and analytical estimate.

Comparing Fig. 20 (a) with the results shown in Fig. 10 and Fig. 11, it can be observed that the maximum RCR of the helicopter rotor is found when the vortex is placed at the outer ends of the rotor disk. When the rotor is handled as a circular fixed-wing, the maximum RCR is obtained when the vortex is located in the middle of the wing. This is because the fixed-wing experiences a constant dynamic pressure all along span, while a rotating blade experiences a dynamic pressure quadratically increasing towards the blade tips. Therefore, when the vortex core is at the blade tip, its largest induced velocities are in the vicinity of the blade tips as well, and cause larger variation of lift than a vortex position at the hub center, where the dynamic pressure and thus resulting forces are very small.

In Fig. 20 (b) the peak values of these four scenarios shown in (a) are then compared to the maximum values of the results shown in Fig. 10 and Fig. 11 for the same distance relative to the WE turbine. First, the circular wing analysis compares surprisingly well with the HOST complete helicopter trim, despite the fact that the fixed-wing aerodynamic treatment is only based on the assumed flight speed of the wing of $V = 20\,m/s$, while the helicopter trim with rotating blades was performed near hover with $V = 2.5\,m/s$. It needs to be checked whether this agreement is accidentally or similar for other flight speeds as well. Second, the HOST RCR is larger than that of the analytical isolated rotor estimate. This is due to the larger collective computed by HOST and also due to the lateral cyclic predicted by HOST, which is zero in the simplified analysis due to the central flapping hinge. The longitudinal control required to compensate the WE vortex effects is found similar between HOST and the simple analysis.

The trend with respect to the strength of the vortex is predicted the same for all three methods: the stronger the vortex, the larger the RCR. In any of the four cases computed, the roll control ratio is found to be 0.25 in maximum and thus it is no problem for the helicopter to compensate the WE vortex effects, at least in steady trim.

5. CONCLUSIONS

In this paper the effect of a wind energy turbine wake vortex on the roll control ratio of a sailplane, a helicopter represented as a circular fixed-wing aircraft, a complete helicopter simulated by HOST, and a simplified analytical treatment of an isolated helicopter rotor are compared. The major conclusions are:

- In 100 m distance to a 3 MW turbine a sailplane flying with a speed of 17 m/s would exceed an RCR of 1 and thus become uncontrollable, because the vortex-induced roll moments cannot be compensated by the controls.
- In the same scenario, a helicopter of Bo105 size represented as a circular fixed-wing aircraft flying at a speed of 20 m/s would not be endangered due to an RCR of about 0.2.
- The complete Bo105 helicopter simulation with rotating blades, fuselage, tail rotor etc. at a flight speed near hover computes the RCR to 0.15, leaving even more margins for control. It is found that the main rotor controls are affected directly by the WE vortex, but also indirectly by an overall affected trim of the entire helicopter.
- The simplified isolated rotor analysis predicts only half of the RCR compared to the complete helicopter simulation. This is partly due to the missing fuselage, tail rotor etc. and their influence on the overall trim.

Future investigations will focus on the helicopter trim when all components of the helicopter are subjected to the WE vortex, and to the flight dynamics response when entering and leaving the WE wake spiral. Also, the WE vortex impact on the helicopter trim will be investigated for different flight speeds of the helicopter.

6. REFERENCES

[1] Schwarz, C.W. Fischenberg, D., "Wake Turbulence Hazard Analysis for a General Aviation Accident," Deutscher Luft- und Raumfahrt Kongress, Augsburg, Germany, Sept.16-18, 2014.

[2] Dunham, R.E., Holbrook, G.T., Mantay, W.R., Campbell, R.L., Van Gunst, R.W., "Flight-Test Experience of a Helicopter Encountering an Airplane Trailing Vortex", 32nd Annual National V/STOL Forum of the American Helicopter Society, Washington, DC, May 10-12, 1976.

[3] Mantay, W.R., Holbrook, G.T., Campbell, R.L. and Tamaine, R.L., "Helicopter response of an airplane's trailing vortex," *Journal of Aircraft*, **14**(4), 1977, pp. 357-363.

[4] Saito, S., Azuma, A., Kawachi, K., Okuno, Y., Hasegawa, T., "Numerical simulations of dynamic response of fixed and rotary wing aircraft to a large airplane wake," 13th European Rotorcraft Forum, Arles, France, Sept. 8-11, 1987.

[5] Azuma, A., Saito, S., Kawachi, K., "Response of a helicopter penetrating the tip vortices of a large airplane," *VERTICA*, **11**(1), 1987, pp. 65-76.

[6] Turner, G.P., Padfield, G.D., Harris, M., "Encounters with Aircraft Vortex Wakes; The Impact on Helicopter Handling Qualities," *Journal of Aircraft*, **39**(5), 2002, pp. 839–849.

[7] Padfield, G.D., Manimala, B., Turner, G.P., "A Severity Analysis for Rotorcraft Encounters with Vortex Wakes," *Journal of the American Helicopter Society*, **49**(4), 2004, pp. 445–456.

[8] Lawrence, B., Padfield, G.D., "Wake Vortex Encounter Severity for Rotorcraft in Approach and Landing," 31st European Rotorcraft Forum, Florence, Italy, Sept. 13-15, 2005.

[9] Leishman, J.G., *Principles of Helicopter Aerodynamics*. Cambridge: Cambridge University Press, UK, 2000.

[10] Burnham, D.C., Hallock, J.N., "Chicago Monostatic Acoustic Vortex Sensing System," U.S. Department of Transportation, DOT-TSC-FAA-79-103, 1982.

[11] Vatistas, G.H., Kozel, V., Mih, W.C., „A Simpler Model for Concentrated Vortices," *Experiments in Fluids*, **11**(1), 1991, pp. 73-76.

[12] Wang, X., White, M., Barakos, G., *Wind Turbine Wake Encounter Study*. Liverpool: University of Liverpool, UK, 2015.

[13] Schwarz, C.W., Hahn, K.-U., "Full-Flight simulator study for wake vortex hazard area investigation," Aerospace Science and Technology, **10**(2), 2006, pp. 136-143.

[14] Barrows, T. M., "Simplified methods of predicting aircraft rolling moments due to vortex encounters," AIAA 14th Aerospace Sciences Meeting, Washington, DC, Jan. 26-28, 1976.

[15] de Bruin, A., "WAVENC, Wake vortex evolution and wake vortex encounter," Synthesis Report, National Aerospace Lab., NLR-TR-2000-079, Amsterdam, Netherlands, 2000.

[16] Fischenberg, D., "A method to validate wake vortex encounter models from flight test data," 27th International Congress of the Aeronautical Sciences, Nice, France, Sept. 19-24, 2010.

[17] Schwarz, C.W., Hahn, K.-U., Fischenberg, D., "Wake Encounter Severity Assessment Based on Validated Aerodynamic Interaction Models," AIAA ASE Conference, Toronto, Canada, Aug. 2-5, 2010.

[18] McCormick, B., Aerodynamics, Aeronautics and Flight Mechanics John Wiley & Sons, Inc. (1995) Canada, 2010.

[19] Benoit, B., Dequin, A.-M., Kampa, K., von Grünhagen, W., Basset, P.-M., Gimonet, B., „HOST, a General Helicopter Simulation Tool for Germany and France", 56th Annual Forum of the American Helicopter Society, Virginia Beach, VA, May 2-4, 2000.

[20] Oseen, C.W., "Über Wirbelbewegung in einer reibenden Flüssigkeit," *Ark. J. Mat. Astron. Fys.*, **7**, 1912, pp. 14-21.

[21] Lamb, H., *Hydrodynamics*, Cambridge: Cambridge University Press, UK, 1932, pp.592-593, 668-669.

[22] Hahn, K.-U., "Coping with Wake Vortex," 23rd International Congress of Aeronautical Sciences, Toronto, Canada, Sept. 8-13, 2002.

[23] Hahn, K.-U., Schwarz, C.W., Friehmelt, H., "A Simplified Hazard Area Prediction (SHAPe) Model for Wake Vortex Encounter Avoidance," 24th International Congress of Aeronautical Sciences, Yokohama, Japan, Aug. 29 - Sept. 3, 2004.

[24] Schwarz, C.W., Hahn, K.-U., "Simplified Hazard Area Prediction Method SHAPe," DLR Institute Report IB 111-2011/31, Braunschweig, Germany, December 2011.

APPENDIX

The derivation of the integrals in Eqs. (24) and (25), based on the kernel function of Eq. (13), are given here.[1] They are divided in two parts. First, the simplified problem for the case of $y_0 = 0$, i.e., a vortex centered in the rotor disk, is solved; second, the general problem for arbitrary position of the vortex axis within or outside the rotor disk is solved. The first goal is to evaluate the Fourier series (exactly: only the constant part and the first sine coefficient) of the following periodic function, which is the kernel of Eq. (13):

$$(28)\quad f:[0;2\pi)\to\Re,\quad f(\psi)=(r+\mu\sin\psi)\frac{r\sin\psi-y_0}{(r\sin\psi-y_0)^2+r_c^{\,2}}=\frac{P(\psi)}{Q(\psi)},\quad r\in(0;1],\ r_c\geq 0,\ y_0\in\mathbb{R}$$

The second goal is the radial integration of these two Fourier coefficients.

A. Simplified problem: exact solution for any core radius, $y_0 = 0$

This results into a simplified form. Define $p = r_c/r \geq 0$.

$$f(\psi)=(r+\mu\sin\psi)\frac{r\sin\psi}{(r\sin\psi)^2+r_c^{\,2}}=\frac{\mu}{r}\frac{\sin^2\psi+\frac{r}{\mu}\sin\psi}{\sin^2\psi+\left(\frac{r_c}{r}\right)^2}=\frac{\mu p}{r_c}\frac{\sin^2\psi+\frac{r_c}{\mu p}\sin\psi}{\sin^2\psi+p^2}$$

(29)

$$=\frac{\mu p}{r_c}\left(1+\frac{\frac{r_c}{\mu p}\sin\psi-p^2}{\sin^2\psi+p^2}\right)$$

The usage of Euler's equation eliminates the sine. Define $z = e^{i\psi}$.

(30)

$$\psi\in\mathbb{C}:\qquad \sin\psi=\frac{1}{2i}\left(e^{i\psi}-e^{-i\psi}\right)=\frac{1}{2i}\left(z-z^{-1}\right)$$

Inserting into Eq. (29) results in:

$$(31)\ f(\psi)=g(z)=\frac{\mu p}{r_c}\left(1+\frac{\frac{r_c}{2i\mu p}\left(z-z^{-1}\right)-p^2}{-\frac{1}{4}\left(z-z^{-1}\right)^2+p^2}\right)=\frac{\mu p}{r_c}\left(1-4\frac{\frac{r_c}{2i\mu p}\left(z^2-1\right)z-p^2z^2}{\left(z^2-1\right)^2-4p^2z^2}\right)$$

The zeros of the denominator are identified in terms of z^2 as

$$(32)\left(z^2-1\right)^2-4p^2z^2=z^4-2\left(1+2p^2\right)z^2+1=0\quad\Rightarrow\quad z_{1,2}^2=1+2p^2\pm\sqrt{\left(1+2p^2\right)^2-1}\in\mathbb{R}$$

It is obvious that due to $p > 0$ one zero $z_1^2 > 1$ and the other $z_2^2 < 1$. Next, the fraction in Eq. (31) is decomposed into partial fractions in order to express it as a power series thereafter. The nominator will be separated into an even and an uneven part of z and both parts will be decomposed separately. Let's begin with the even part:

[1] They have been derived by Lennert van der Wall, at that time student in the Master's program of Electrical Engineering, TU Braunschweig

$$\frac{-z^2}{\left(z^2-1\right)^2-4p^2}=\frac{-z^2}{\left(z^2-z_1^2\right)\left(z^2-z_2^2\right)}=\frac{\frac{-z_1^2}{z_1^2-z_2^2}}{z^2-z_1^2}+\frac{\frac{-z_2^2}{z_2^2-z_1^2}}{z^2-z_2^2}$$

(33)
$$=\frac{1}{z_1^2-z_2^2}\left(-z_1^2\frac{1}{z^2-z_1^2}+z_2^2\frac{1}{z^2-z_2^2}\right)=\frac{1}{z_1^2-z_2^2}\left(\frac{1}{1-\left(\frac{z}{z_1}\right)^2}+\left(\frac{z_2}{z}\right)^2\frac{1}{1-\left(\frac{z_2}{z}\right)^2}\right)$$

$$=\frac{1}{z_1^2-z_2^2}\left(\sum_{k=0}^{\infty}\left(\frac{z}{z_1}\right)^{2k}+\left(\frac{z_2}{z}\right)^2\sum_{k=0}^{\infty}\left(\frac{z_2}{z}\right)^{2k}\right),\qquad \left|z^2\right|\overset{!}{<}z_1^2\quad\wedge\quad\left|z^2\right|\overset{!}{>}z_2^2$$

The partial fractions are transformed into a power series. Define $q\in\mathbb{C},|q|<1$.

(34)
$$\frac{1}{1-q}=\sum_{k=0}^{\infty}q^k$$

Care must be taken to ensure that $z=e^{i\psi}$ remains in both ranges of convergence because otherwise the geometric series does not make sense in this context. Therefore both summands are factored differently. A further simplification is obtained by the relation $z_2^2=1/z_1^2$. Then, Eq. (33) becomes

$$\frac{-z^2}{\left(z^2-1\right)^2-4p^2}=\frac{1}{z_1^2-z_2^2}\left(\sum_{k=0}^{\infty}\left(z_2z\right)^{2k}+\left(\frac{z_2}{z}\right)^2\sum_{k=0}^{\infty}\left(\frac{z_2}{z}\right)^{2k}\right)$$

(35)
$$=\frac{1}{z_1^2-z_2^2}\left(1+\sum_{k=0}^{\infty}\left(z_2z\right)^{2k}+\sum_{k=0}^{\infty}\left(\frac{z_2}{z}\right)^{2k+2}\right)$$

$$=\frac{1}{z_1^2-z_2^2}\left(1+\sum_{k=0}^{\infty}z_2^{2k}\left(z^{2k}+z^{-2k}\right)\right)\qquad\text{with:}\quad\cos\left(2k\psi\right)=\frac{z^{2k}+z^{-2k}}{2}$$

$$=\frac{1}{z_1^2-z_2^2}\left(1+2\sum_{k=0}^{\infty}z_2^{2k}\cos\left(2k\psi\right)\right)$$

Now the uneven part is treated in the same manner. One z can be factored out that is not needed for the partial fraction decomposition. Remember that $z_2^2=1/z_1^2$.

$$\frac{\left(z^2-1\right)z}{\left(z^2-1\right)^2-4p^2}=\frac{z}{z_1^2-z_2^2}\left(\frac{z_1^2-1}{z^2-z_1^2}-\frac{z_2^2-1}{z^2-z_2^2}\right)=\frac{z}{z_1^2-z_2^2}\left(\frac{z_1^2-1}{-z_1^2}\frac{1}{1-\left(\frac{z}{z_1}\right)^2}-\frac{z_2^2-1}{z^2}\frac{1}{1-\left(\frac{z_2}{z}\right)^2}\right)$$

(36)
$$=z\frac{z_2^2-1}{z_1^2-z_2^2}\left(\sum_{k=0}^{\infty}\left(\frac{z}{z_1}\right)^{2k}-\frac{1}{z^2}\sum_{k=0}^{\infty}\left(\frac{z_2}{z^2}\right)^{k}\right),\qquad z_2^2\overset{!}{<}\left|z^2\right|\overset{!}{<}z_1^2$$

$$=\frac{z_2^2-1}{z_1^2-z_2^2}\sum_{k=0}^{\infty}z_2^{2k}\left(z^{2k+1}-z^{-2k-1}\right)\qquad\text{with:}\quad\sin\left(\left(2k+1\right)\psi\right)=\frac{z^{2k+1}-z^{-2k-1}}{2i}$$

$$=2i\frac{z_2^2-1}{z_1^2-z_2^2}\sum_{k=0}^{\infty}z_2^{2k}\sin\left(\left(2k+1\right)\psi\right)$$

Both partial fraction decompositions Eqs. (35) and (36) provide the desired Fourier series expansion of Eq. (28).

$$
\begin{aligned}
f(\psi) &= \frac{\mu p}{r_c}\left\{1-4\left[\frac{r_c}{\cancel{2i}\,\mu p}\,\cancel{2i}\,\frac{z_2^2-1}{z_1^2-z_2^2}\sum_{k=0}^{\infty} z_2^{2k}\sin\left((2k+1)\psi\right)+p^2\frac{1}{z_1^2-z_2^2}\left(1+2\sum_{k=0}^{\infty} z_2^{2k}\cos\left(2k\psi\right)\right)\right]\right\} \\
&= \frac{\mu p}{r_c}\left(1-\frac{4p^2}{z_1^2-z_2^2}\right)-\frac{4}{z_1^2-z_2^2}\left[\left(z_2^2-1\right)\sum_{k=0}^{\infty} z_2^{2k}\sin\left((2k+1)\psi\right)+\frac{2\mu p^3}{r_c}\sum_{k=0}^{\infty} z_2^{2k}\cos\left(2k\psi\right)\right]
\end{aligned}
\tag{37}
$$

Comparing this result with the coefficients of a normal Fourier series the requires steady a_0 and fundamental sine b_1 coefficients are identified. The following substitutions provide the result only in terms of the radial coordinate r, and the core radius r_c

$$
z_1^2-z_2^2 = 2\sqrt{\left(1-2p^2\right)^2-1} = 4p\sqrt{1+p^2} \qquad \text{and} \qquad p=\frac{r_c}{r}\in\left(r_c,\infty\right) \tag{38}
$$

Then:

$$
\begin{aligned}
a_0 &= \frac{\mu p}{r_c}\left(1-\frac{2p^2}{\sqrt{\left(1+2p^2\right)^2-1}}\right)=\frac{\mu p}{r_c}\left(1-\frac{p}{\sqrt{1+p^2}}\right)=\frac{\mu}{r}\left(1-\frac{1}{\sqrt{1+\left(r/r_c\right)^2}}\right) \\
b_1 &= 2\frac{\cancel{1}+2p^2-\sqrt{\left(1+2p^2\right)^2-1}\cancel{-1}}{\sqrt{\left(1+2p^2\right)^2-1}}=2\left(1-\frac{2p^2}{\sqrt{\left(1+2p^2\right)^2-1}}\right)=2\left(1-\frac{1}{\sqrt{1+\left(r/r_c\right)^2}}\right)
\end{aligned}
\tag{39}
$$

Finally, the integrals with respect to the radial coordinate can be solved and then evaluated for the upper and lower bounds B and A. Define $x = r/r_c$.

$$
\begin{aligned}
\int a_0\,dr &= \mu\int\frac{1}{x\,\cancel{r_c}}\left(1-\frac{1}{\sqrt{1+x^2}}\right)\cancel{r_c}\,dx=\mu\ln\left(1+\sqrt{1+x^2}\right)=\mu\ln\left(1+\sqrt{1+\left(r/r_c\right)^2}\right) \\
\int b_1 r\,dr &= 2\int x r_c\left(1-\frac{1}{\sqrt{1+x^2}}\right)r_c\,dx=2r_c^{\,2}\left(\frac{x^2}{2}-\sqrt{1+x^2}\right)=r^2-r_c^{\,2}\sqrt{1+\left(r/r_c\right)^2}
\end{aligned}
\tag{40}
$$

B. Exact solution for any core radius and arbitrary lateral vortex position

Using the abbreviations $a = y_0/r \in \mathbb{R}$ and $b = r_c/r \geq 0$ the general form of Eq. (28) becomes

$$
\begin{aligned}
f(\psi) &= (1+\mu\sin\psi)\frac{r\sin\psi - y_0}{(r\sin\psi - y_0)^2 + r_c^2} = \frac{\mu}{r}\left(\sin\psi + \frac{r}{\mu} \mp a\right)\frac{\sin\psi - a}{(\sin\psi - a)^2 + b^2} \\
&= \frac{\mu}{r}\left[\frac{(\sin\psi - a)^2}{(\sin\psi - a)^2 + b^2} + \left(a + \frac{r}{\mu}\right)\frac{\sin\psi - a}{(\sin\psi - a)^2 + b^2}\right] \\
&= \frac{\mu}{r}\left[1 - \frac{b^2}{(\sin\psi - a)^2 + b^2} + \left(a + \frac{r}{\mu}\right)\frac{\sin\psi - a}{(\sin\psi - a)^2 + b^2}\right]
\end{aligned}
\tag{41}
$$

A substitution $\sin\psi \to x \in \mathbb{C}$ is followed by a partial fraction decomposition and the zeros are obtained from the quadratic terms in x, where $x_{1,2} = a \pm ib$ and thus $x_2 = x_1^*$ is the conjugate complex of x_1.

$$
\begin{aligned}
\frac{b}{(x-a)^2 + b^2} &= \frac{b}{(x - x_1)(x - x_1^*)} = \frac{1}{2i}\left(\frac{1}{x - x_1} - \frac{1}{x - x_1^*}\right) \\
\frac{x-a}{(x-a)^2 + b^2} &= \frac{x-a}{(x - x_1)(x - x_1^*)} = \frac{1}{2}\left(\frac{1}{x - x_1} + \frac{1}{x - x_1^*}\right)
\end{aligned}
\tag{42}
$$

Now x is re-substituted and instead Euler's equation for the sine is introduced into the first of the partial fraction.

$$
\begin{aligned}
x \to \sin\psi &= \frac{1}{2i}\left(e^{i\psi} - e^{-i\psi}\right) = \frac{1}{2i}\left(z - z^{-1}\right) \\
\Rightarrow \quad \frac{1}{2i}\frac{1}{x - x_1} &= \frac{z}{(z^2 - 1) - 2ix_1 z} = \frac{z}{z^2 - 2ix_1 z - 1} = \frac{z}{(z - z_1)(z - z_2)}
\end{aligned}
\tag{43}
$$

The zeros have the following characteristics:

$$
z_1 z_2 = -1 \quad \Rightarrow \quad z_{1,2} \neq 0 \quad \text{and} \quad |z_1| = \frac{1}{|z_2|} \neq 1 \quad \Rightarrow \quad |z_1| > 1 > |z_2|
\tag{44}
$$

By definition $|z_1|$ is chosen as the larger zero. $|z_1| \neq 1$ is valid since otherwise a solution with $Q(\psi) = 0$ would be possible in Eq. (28) for $\psi \in \mathbb{R}$ and due to $r_c > 0$ this never is the case. The coefficients of the quadratic to compute the zeros $z_{1,2}$ are complex and therefore a Cartesian representation of the root of a complex number is needed.

$$
z = a + ib \in \mathbb{C} \quad \Rightarrow \quad \sqrt{z} = \pm\left(\operatorname{sgn}(b)\sqrt{\frac{|z| + a}{2}} + i\sqrt{\frac{|z| - a}{2}}\right)
\tag{45}
$$

The sign of $\sqrt{z}$ is not a $\pm$ because, following Moivre's formula for $n = 2$, the root of a complex number contains both solutions already. Thus, using Eq. (45) the zeros are:

(46)

$$z_{1,2} = ix_1 + \sqrt{1-x_1^2}$$

$$= -b + ia \pm \left[\operatorname{sgn}(-2ab) \sqrt{\frac{\left|1-x_1^2\right| + \left(1-a^2+b^2\right)}{2}} + i\sqrt{\frac{\left|1-x_1^2\right| - \left(1-a^2+b^2\right)}{2}} \right]$$

$$= -\operatorname{sgn}(b) \left[|b| \pm \operatorname{sgn}(a) \sqrt{\frac{\left|1-x_1^2\right| + \left(1-a^2+b^2\right)}{2}} \right] + i \operatorname{sgn}(a) \left[|a| \pm \operatorname{sgn}(a) \sqrt{\frac{\left|1-x_1^2\right| - \left(1-a^2+b^2\right)}{2}} \right]$$

$$= -\operatorname{sgn}(b) \left[|b| \pm \sqrt{\frac{\left|1-x_1^2\right| + \left(1-a^2+b^2\right)}{2}} \right] + i \operatorname{sgn}(a) \left[|a| \pm \sqrt{\frac{\left|1-x_1^2\right| - \left(1-a^2+b^2\right)}{2}} \right]$$

In the last line a rearrangement for the cases $a < 0$ was done. It is easy to prove that $|z_1| > |z_2|$ because the roots and absolute values add for z_1 while for z_2 they compensate in parts. The other partial fraction $1/\left(2i(x - x_1^*)\right)$ becomes

(47) $$z_{3,4} = -z_{1,2}^* \qquad | \, b \to -b \qquad \Rightarrow \qquad \Re\{\,\} \to -\Re\{\,\},\ \Im\{\,\} \text{ remains}$$

Using the zeros z_1 to z_4 and the geometrical series Eq. (34) the partial fractions can be represented as a power series. Again it is necessary to ensure that $z = e^{i\psi}$ is inside all convergence areas such that the power series is valid.

$$\frac{1}{2i}\frac{1}{x-x_1} = \frac{z}{(z-z_1)(z-z_2)} = \frac{1}{z_1-z_2}\left(\frac{z_1}{z-z-1} - \frac{z_2}{z-z_2}\right) = \frac{1}{z_1-z_2}\underbrace{\left(-\sum_{k=0}^{\infty}\frac{z^k}{z_1^k} - \frac{z_2}{z}\sum_{k=0}^{\infty}\frac{z_2^k}{z^k}\right)}_{|z|\overset{!}{<}|z_1| \,\wedge\, |z|\overset{!}{>}|z_2|}$$

(48) $$= \frac{1}{z_2-z_1}\left[1 + \sum_{k=0}^{\infty}\left(-z_2\right)^k z^k + z_2^k z^{-k}\right] \qquad \text{with} \quad z_1 = -\frac{1}{z_2}$$

and $$\frac{1}{2i}\frac{1}{x-x_1^*} = \frac{z}{(z-z_3)(z-z_4)} = \frac{1}{z_2^*-z_1^*}\left[1 + \sum_{k=0}^{\infty}\left(z_2^*\right)^k z^k + \left(-z_2^*\right)^k z^{-k}\right] \qquad \text{with} \quad z_{3,4} = -z_{1,2}^*$$

Via the series representation of the partial fractions finally the desired Fourier series $f(\psi)$ is obtained. The first contribution to $f(\psi)$ stems from the first partial fraction. Recall that $z = e^{i\psi}$.

$$\frac{b}{(x-a)^2+b^2} = \frac{1}{2i}\left(\frac{1}{x-x_1} - \frac{1}{x-x_1^*}\right)$$

(49) $$= \left(\frac{1}{z_2-z_1} + \frac{1}{z_2^*-z_1^*}\right) + \sum_{k=1}^{\infty}\left\{\underbrace{\left[\frac{\left(-z_2\right)^k}{z_2-z_1} + \frac{\left(z_2^*\right)^k}{z_2^*-z_1^*}\right]}_{=:u_k - iv_k} z^k + \underbrace{\left[\frac{z_2^k}{z_2-z_1} - \frac{\left(-z_2^*\right)^k}{z_2^*-z_1^*}\right]}_{=:u_k + iv_k} z^{-k}\right\}$$

$$= u_0 + 2\sum_{k=1}^{\infty}\left[u_k \cos k\psi - iv_k\left(i \sin k\psi\right)\right]$$

$$= u_0 + 2\sum_{k=1}^{\infty}\left(u_k \cos k\psi + v_k \sin k\psi\right)$$

The second contribution to $f(\psi)$ stems from the second partial fraction.

$$\frac{x-a}{(x-a)^2+b^2}=\frac{1}{2}\left(\frac{1}{x-x_1}+\frac{1}{x-x_1^*}\right)$$

$$=i\left(\frac{1}{z_2-z_1}-\frac{1}{z_2^*-z_1^*}\right)+\sum_{k=1}^{\infty}\left\{\underbrace{\left[\frac{(-z_2)^k}{z_2-z_1}-\frac{(z_2^*)^k}{z_2^*-z_1^*}\right]}_{=:\frac{1}{i}(u_k'-iv_k')}z^k+\underbrace{\left[\frac{z_2^k}{z_2-z_1}-\frac{(-z_2^*)^k}{z_2^*-z_1^*}\right]}_{=:\frac{1}{i}(u_k'+iv_k')}z^{-k}\right\} \tag{50}$$

$$=u_0'+2\sum_{k=1}^{\infty}\left[u_k'\cos k\psi-iv_k'\left(i\sin k\psi\right)\right]$$

$$=u_0'+2\sum_{k=1}^{\infty}\left(u_k'\cos k\psi+v_k'\sin k\psi\right)$$

Both Eqs. (49) and (50) together provide the desired resulting Fourier series of Eq. (41), of which only the constant and the first sine term are needed.

$$f(\psi)=\frac{\mu}{r}\left[1-b\left(u_0+2\sum_{k=1}^{\infty}\left(u_k\cos k\psi+v_k\sin k\psi\right)\right)+\left(a+\frac{r}{\mu}\right)\left(u_0'+2\sum_{k=1}^{\infty}\left(u_k'\cos k\psi+v_k'\sin k\psi\right)\right)\right] \tag{51}$$

$$=:a_0+\sum_{k=1}^{\infty}\left(a_k\cos k\psi+b_k\sin k\psi\right)$$

The abbreviations used therein are repeated here: $a:=y_0/r\in\mathbb{R}$; $b:=r_c/r\geq 0$ and $x_1:=a+ib$. It follows that

$$z_{1,2}:=-\operatorname{sgn}(b)\left[|b|\pm\sqrt{\frac{\left|1-x_1^2\right|+\left(1-a^2+b^2\right)}{2}}\right]+i\operatorname{sgn}(a)\left[|a|\pm\sqrt{\frac{\left|1-x_1^2\right|+\left(1-a^2+b^2\right)}{2}}\right] \tag{52}$$

$$\Rightarrow\quad u_k+iv_k:=\frac{z_2^k}{z_2-z_1}+\frac{(-z_2^*)^k}{z_2^*-z_1^*}\qquad\text{and}\qquad u_k'+iv_k':=i\left[\frac{z_2^k}{z_2-z_1}-\frac{(-z_2^*)^k}{z_2^*-z_1^*}\right]$$

Depending on k, one of the coefficients u_k, v_k and u'_k, v'_k is always vanishing, because

$$k\text{ even:}\quad v_k=v_k'=0,\qquad u_k=2\Re\left(\frac{z_2^k}{z_2-z_1}\right),\qquad u_k'=-2\Im\left(\frac{z_2^k}{z_2-z_1}\right) \tag{53}$$

$$k\text{ uneven:}\quad u_k=u_k'=0,\qquad v_k=2\Im\left(\frac{z_2^k}{z_2-z_1}\right),\qquad v_k'=2\Re\left(\frac{z_2^k}{z_2-z_1}\right)$$

By comparison of the Fourier coefficients the desired constant and first sine term become

$$a_0=\frac{\mu}{r}\left[1-bu_0+\left(a+\frac{r}{\mu}\right)u_0'\right]\qquad\text{and}\qquad b_1=\frac{2\mu}{r}\left[-bv_1+\left(a+\frac{r}{\mu}\right)v_1'\right] \tag{54}$$

B.1. Radial integration of the coefficient a_0

By back-substitution of a, b and x_1 the coefficient is further simplified with the goal of analytically integrating over the radial coordinate r. It is important to recall that both a, b and with them also x_1 only depend on $1/r$. Thus, expanding with r especially the terms $z_{1,2}$ can be merged together. Expanding with the complex conjugate and then with $r>0$ indeed the dual fractions in r can be eliminated.

Recall that $\zeta := r^2 - {y_0}^2 + {r_c}^2$ is a variable and $\eta := 2|y_0 r_c|$ is a constant, thus x is the only variable in terms of r.

$$u_o - iu_0' = \frac{2}{z_2 - z_1} = r\left[\operatorname{sgn}(r_c)\sqrt{\frac{\sqrt{\zeta^2+\eta^2}+\zeta}{2\left(\zeta^2+\eta^2\right)}} + i\operatorname{sgn}(y_0)\sqrt{\frac{\sqrt{\zeta^2+\eta^2}-\zeta}{2\left(\zeta^2+\eta^2\right)}}\right] \tag{55}$$

By u_0 and u'_0 in Eq. (54) a compact and explicit representation of the coefficient a_0 in dependence of r is obtained.

$$\begin{aligned} a_0 &= \frac{\mu}{r}\left[1 - bu_0 + \left(a + \frac{r}{\mu}\right)u_0'\right] \\ &= \frac{\mu}{r}\left[1 - |r_c|\sqrt{\frac{\sqrt{\zeta^2+\eta^2}+\zeta}{2\left(\zeta^2+\eta^2\right)}} - \left(|y_0| + \operatorname{sgn}(y_0)\frac{r^2}{\mu}\right)\sqrt{\frac{\sqrt{\zeta^2+\eta^2}-\zeta}{2\left(\zeta^2+\eta^2\right)}}\right] \end{aligned} \tag{56}$$

The first of the summands can directly be integrated with respect to r and the other two require a further substitution such as $\zeta := \eta \sinh z$. The idea behind this substitution is that both roots are vanishing.

$$z > 0: \quad \zeta =: \eta \sinh\left(\ln\left(z^2\right)\right) \quad \Rightarrow \quad 2r =: \eta \cosh\left(\ln\left(z^2\right)\right)\frac{2}{z}\frac{dz}{dr} \quad dr =: \eta \cosh\left(\ln\left(z^2\right)\right)\frac{dz}{zr} \tag{57}$$

Further consequences of the substitution are

$$\begin{aligned} z &= \sqrt{e^{\operatorname{arsinh}\frac{\zeta}{\eta}}} = \sqrt{\frac{\sqrt{\zeta^2+\eta^2}+\zeta}{\eta}} \\ \sqrt{\frac{\sqrt{\zeta^2+\eta^2}+\zeta}{2\left(\zeta^2+\eta^2\right)}} &= \frac{1}{\sqrt{2\eta}}\frac{z}{\cosh\ln\left(z^2\right)}; \qquad \sqrt{\frac{\sqrt{\zeta^2+\eta^2}-\zeta}{2\left(\zeta^2+\eta^2\right)}} = \frac{1}{\sqrt{2\eta}}\frac{z^{-1}}{\cosh\ln\left(z^2\right)} \end{aligned} \tag{58}$$

Inserting the substitution all terms with cosh cancel each other and in the last summand the r^2 is vanishing as well. Thus, a direct integration is now possible.

$$\begin{aligned} \int a_0\,dr &= \mu\ln r - \frac{\mu\eta}{\sqrt{2\eta}}\int\frac{1}{r^2 z}\left[|r_c|z + \left(|y_0| + \operatorname{sgn}(y_0)\frac{r^2}{\mu}\right)z^{-1}\right]dz \\ &= \mu\ln r + \operatorname{sgn}(y_0)\sqrt{\frac{\eta}{2}}z^{-1} - \eta\sqrt{\frac{\eta}{2}}\int\frac{1}{r^2 z}\left(|r_c|z + |y_0|z^{-1}\right)dz \\ &= \mu\ln r + \operatorname{sgn}(y_0)\sqrt{\frac{\eta}{2}}\sqrt{\frac{\eta}{\sqrt{\zeta^2+\eta^2}+\zeta}} - \eta\sqrt{\frac{\eta}{2}}\int\frac{1}{r^2 z}\left(|r_c|z + |y_0|z^{-1}\right)dz \\ &= \mu\ln r + y_0\frac{\sqrt{2}|r_c|}{\sqrt{\sqrt{\zeta^2+\eta^2}+\zeta}} - \eta\sqrt{\frac{\eta}{2}}\int\frac{1}{r^2 z}\left(|r_c|z + |y_0|z^{-1}\right)dz \end{aligned} \tag{59}$$

The remaining integral and another one similar to it will be needed later as well, therefore it is separately solved. The following relations are helpful for the rest.

$$\int \frac{1}{r}\left(|r_c| \sqrt{\frac{\sqrt{\zeta^2+\eta^2}+\zeta}{2\left(\zeta^2+\eta^2\right)}} + |y_0| \sqrt{\frac{\sqrt{\zeta^2+\eta^2}-\zeta}{2\left(\zeta^2+\eta^2\right)}} \right) dr = \frac{\eta}{\sqrt{2\eta}} \int \frac{1}{r^2 z} \left(|r_c| z + |y_0| z^{-1} \right) dz$$

(60)

$$\int \frac{1}{r}\left(|y_0| \sqrt{\frac{\sqrt{\zeta^2+\eta^2}+\zeta}{2\left(\zeta^2+\eta^2\right)}} - |r_c| \sqrt{\frac{\sqrt{\zeta^2+\eta^2}-\zeta}{2\left(\zeta^2+\eta^2\right)}} \right) dr = \frac{\eta}{\sqrt{2\eta}} \int \frac{1}{r^2 z} \left(|y_0| z - |r_c| z^{-1} \right) dz$$

For the rest the r^2 in any terms with x needs to be substituted for z. The following theorem is needed to proceed: $\operatorname{arctanh} z = \operatorname{arctanh} z^{-1}$.

$$\sqrt{\frac{\eta}{2}} \int \frac{1}{r^2 z} \left(|r_c| z + |y_0| z^{-1} \right) dz = \sqrt{\frac{\eta}{2}} \frac{|r_c|}{\eta/2} \int \frac{z^2 + \left| \frac{y_0}{r_c} \right|}{z^4 + 2\frac{{y_0}^2 - {r_c}^2}{\eta} z^2 - 1} dz$$

(61)

$$= \sqrt{\left| \frac{r_c}{y_0} \right|} \int \frac{z^2 + \left| \frac{y_0}{r_c} \right|}{\left(z^2 + \left| \frac{y_0}{r_c} \right| \right)\left(z^2 - \left| \frac{r_c}{y_0} \right| \right)} dz = -\sqrt{\left| \frac{r_c}{y_0} \right|} \left| \frac{y_0}{r_c} \right| \int \frac{1}{1 - \left| \frac{y_0}{r_c} \right| z^2} dz$$

$$= -\sqrt{\left| \frac{y_0}{r_c} \right|} \sqrt{\left| \frac{r_c}{y_0} \right|} \operatorname{ar\,tanh}\left(\sqrt{\left| \frac{y_0}{r_c} \right|} z \right) = -\operatorname{ar\,tanh}\left(\sqrt{\left| \frac{r_c}{y_0} \right|} z^{-1} \right)$$

$$= -\operatorname{ar\,tanh}\left(\sqrt{\left| \frac{r_c}{y_0} \right|} \sqrt{\frac{\eta}{\sqrt{\zeta^2+\eta^2}+\zeta}} \right) = -\operatorname{ar\,tanh}\left(\frac{\sqrt{2}|r_c|}{\sqrt{\sqrt{\zeta^2+\eta^2}+\zeta}} \right)$$

The second integral of Eq. (60) is solved in the same manner and the following theorem is needed now: $\tan^{-1} z = -\tan^{-1} z^{-1} \pm \pi/2$. The result is:

(62)
$$\sqrt{\frac{\eta}{2}} \int \frac{1}{r^2 z} \left(|y_0| z - |r_c| z^{-1} \right) dz = -\arctan\left(\frac{\sqrt{2}|y_0|}{\sqrt{\sqrt{\zeta^2+\eta^2}+\zeta}} \right)$$

Combining Eq. (59) with Eqs. (61) and (62) finally provides the desired result. It is easy to prove the correctness by derivation with respect to r.

(63)
$$\int a_0 \, dr = \mu \ln r + y_0 \frac{\sqrt{2}|r_c|}{\sqrt{\sqrt{\zeta^2+\eta^2}+\zeta}} + \mu \operatorname{ar\,tanh}\left(\frac{\sqrt{2}|r_c|}{\sqrt{\sqrt{\zeta^2+\eta^2}+\zeta}} \right)$$

Recall that therein $\zeta = r^2 - {y_0}^2 + {r_c}^2$ and $\eta = 2|y_0 r_c|$. However, this representation is numerically unstable for $r \to 0$ because the first term approaches $-\infty$ and the second $+\infty$. These terms cancel each other, but this is not immediately apparent. A re-arrangement eliminates this problem and after some further steps the following result is obtained that is free of this instability. Again, it is easy to prove the correctness by derivation with respect to r.[2]

[2] Note that during the derivation a constant part $-(\mu/2)\ln 2$ was added to the general integration constant. Therefore the values of the Eqs. (63) and (64) are not identical in the limit $r \to 0$.

(64) $$\int a_0\,dr = \mu \ln\sqrt{\sqrt{\zeta^2+\eta^2}+\zeta+2{y_0}^2} + \mu \ln\left(1+\frac{\sqrt{2}\,|r_c|}{\sqrt{\sqrt{\zeta^2+\eta^2}+\zeta}}\right) + y_0\frac{\sqrt{2}\,|r_c|}{\sqrt{\sqrt{\zeta^2+\eta^2}+\zeta}}$$

B.2. Radial integration of the product rb_1

With the results obtained during the derivation beforehand this is not a large problem anymore.

(65) $$b_1 = \frac{2\mu}{r}\left[-bv_1+\left(a+\frac{r}{\mu}\right)v_1'\right]; \qquad v_1'+iv_1 = \frac{2z_2}{z_2-z_1}$$

The results of Eq. (55) can be used and by expansion with r the dual fractions can be eliminated. This results in the already known square root terms, wherein x and y are defined as before.

(66) $$\begin{aligned} v_1'+iv_1 = \frac{2z_2}{z_2-z_1} &= 1-|r_c|\sqrt{\frac{\sqrt{\zeta^2+\eta^2}+\zeta}{2\left(\zeta^2+\eta^2\right)}}-|y_0|\sqrt{\frac{\sqrt{\zeta^2+\eta^2}-\zeta}{2\left(\zeta^2+\eta^2\right)}} \\ &+i\,\mathrm{sgn}\left(y_0 r_c\right)\left[|y_0|\sqrt{\frac{\sqrt{\zeta^2+\eta^2}+\zeta}{2\left(\zeta^2+\eta^2\right)}}-|r_c|\sqrt{\frac{\sqrt{\zeta^2+\eta^2}-\zeta}{2\left(\zeta^2+\eta^2\right)}}\right] \end{aligned}$$

Now the explicit representation of the first sine coefficient of the Fourier series is

(67) $$\begin{aligned} b_1 &= \frac{2\mu}{r}\left[-bv_1+\left(a+\frac{r}{\mu}\right)v_1'\right] \\ &= \frac{2\mu}{r^2}\left[-\mathrm{sgn}\left(y_0\right)|r_c|\left(|y_0|\sqrt{\frac{\sqrt{\zeta^2+\eta^2}+\zeta}{2\left(\zeta^2+\eta^2\right)}}-|r_c|\sqrt{\frac{\sqrt{\zeta^2+\eta^2}-\zeta}{2\left(\zeta^2+\eta^2\right)}}\right)\right] \\ &+\frac{2\mu}{r^2}\left(y_0+\frac{r^2}{\mu}\right)\left[1-|r_c|\sqrt{\frac{\sqrt{\zeta^2+\eta^2}+\zeta}{2\left(\zeta^2+\eta^2\right)}}-|y_0|\sqrt{\frac{\sqrt{\zeta^2+\eta^2}-\zeta}{2\left(\zeta^2+\eta^2\right)}}\right] \end{aligned}$$

The product rb_1 needs to be integrated, which eliminates the square in the denominator of the leading fraction. The term with “1” in the last line can easily be integrated and the major parts of the remaining terms have already been solved before in Eq. (60).

(68) $$\begin{aligned} \int rb_1 dr = 2\mu\Bigg[&\mathrm{sgn}\left(y_0\right)|r_c|\arctan\frac{\sqrt{2}\,|y_0|}{\sqrt{\zeta^2+\eta^2}+\zeta}+y_0\ln r+y_0\,\mathrm{ar\,tanh}\frac{\sqrt{2}r_c}{\sqrt{\zeta^2+\eta^2}+\zeta}\Bigg] \\ &+r^2-2\int r\left[|r_c|\sqrt{\frac{\sqrt{\zeta^2+\eta^2}+\zeta}{2\left(\zeta^2+\eta^2\right)}}+|y_0|\sqrt{\frac{\sqrt{\zeta^2+\eta^2}-\zeta}{2\left(\zeta^2+\eta^2\right)}}\right]dr \end{aligned}$$

The substitution for z is applied to the remaining integral.

$$z>0: \quad \zeta =: \eta \sinh \ln\left(z^2\right) \quad \Rightarrow \quad 2r =: \eta \cosh \ln\left(z^2\right)\frac{2}{z}\frac{dz}{dr}, \quad dr =: \eta \cosh \ln\left(z^2\right)\frac{dz}{rz}$$

(69)
$$\Rightarrow \quad z=\sqrt{e^{\operatorname{arsinh}\frac{\zeta}{\eta}}}=\sqrt{\frac{\sqrt{\zeta^2+\eta^2}+\zeta}{\eta}}, \quad \sqrt{\frac{\sqrt{\zeta^2+\eta^2}+\zeta}{2\left(\zeta^2+\eta^2\right)}}=\frac{1}{\sqrt{2\eta}}\frac{z}{\cosh \ln\left(z^2\right)},$$

$$\text{and} \quad \sqrt{\frac{\sqrt{\zeta^2+\eta^2}-\zeta}{2\left(\zeta^2+\eta^2\right)}}=\frac{1}{\sqrt{2\eta}}\frac{z^{-1}}{\cosh \ln\left(z^2\right)}$$

After insertion into the integral the terms with cosh cancel each other and the integral can be solved.

$$2\int r\left[\left|r_c\right|\sqrt{\frac{\sqrt{\zeta^2+\eta^2}+\zeta}{2\left(\zeta^2+\eta^2\right)}}+\left|y_0\right|\sqrt{\frac{\sqrt{\zeta^2+\eta^2}-\zeta}{2\left(\zeta^2+\eta^2\right)}}\right]dr = 2\frac{\eta}{\sqrt{2\eta}}\int\frac{r}{rz}\left(\left|r_c\right|z+\left|y_0\right|z^{-1}\right)dz$$

$$= \sqrt{2\eta}\left(\left|r_c\right|z-\left|y_0\right|z^{-1}\right)$$

(70)
$$= \sqrt{2\eta}\left(\left|r_c\right|\sqrt{\frac{\sqrt{\zeta^2+\eta^2}+\zeta}{\eta}}-\left|y_0\right|\sqrt{\frac{\eta}{\sqrt{\zeta^2+\eta^2}+\zeta}}\right)$$

$$= \sqrt{2\eta}\left(\left|r_c\right|\sqrt{\frac{\sqrt{\zeta^2+\eta^2}+\zeta}{\eta}}-\left|y_0\right|\sqrt{\frac{\sqrt{\zeta^2+\eta^2}-\zeta}{\eta}}\right)$$

$$= \sqrt{2}\left(\left|r_c\right|\sqrt{\sqrt{\zeta^2+\eta^2}+\zeta}-\left|y_0\right|\sqrt{\sqrt{\zeta^2+\eta^2}-\zeta}\right)$$

With this and Eq. (68) the final result is obtained.

(71)
$$\int rb_1\,dr = 2\mu\left[\operatorname{sgn}\left(y_0\right)\left|r_c\right|\arctan\frac{\sqrt{2}\left|y_0\right|}{\sqrt{\zeta^2+\eta^2}+\zeta}+y_0\ln r+y_0\operatorname{ar\,tanh}\frac{\sqrt{2}r_c}{\sqrt{\zeta^2+\eta^2}+\zeta}\right]$$
$$+r^2-\sqrt{2}\left(\left|r_c\right|\sqrt{\sqrt{\zeta^2+\eta^2}+\zeta}-\left|y_0\right|\sqrt{\sqrt{\zeta^2+\eta^2}-\zeta}\right)$$

Of course, the same numerical instability as for the former result is present and a transformation is needed to eliminate this in the same manner as before. Then, the numerically stable final result is obtained.

$$\int rb_1\,dr = 2\mu\operatorname{sgn}\left(y_0\right)\left|r_c\right|\arctan\frac{\sqrt{2}\left|y_0\right|}{\sqrt{\zeta^2+\eta^2}+\zeta}$$

(72)
$$+2\mu y_0\left[\ln\sqrt{\sqrt{\zeta^2+\eta^2}+\zeta+2y_0{}^2}+\ln\left(1+\frac{\sqrt{2}\left|r_c\right|}{\sqrt{\sqrt{\zeta^2+\eta^2}+\zeta}}\right)\right]$$
$$+r^2-\sqrt{2}\left(\left|r_c\right|\sqrt{\sqrt{\zeta^2+\eta^2}+\zeta}-\left|y_0\right|\sqrt{\sqrt{\zeta^2+\eta^2}-\zeta}\right)$$

It can easily be shown that for $y_0 = 0$ the same result is obtained as for the simplified solution given in Eqs. (24) and (25).